JOURNAL OF GEOPHYSICAL RESEARCH, VOL. 108, NO. A11, 1410, doi:10.1029/2003JA009849, 2003

Acceleration of coronal mass ejections

James Chen and Jonathan Krall
Plasma Physics Division, Naval Research Laboratory, Washington, DC, USA

Received 16 January 2003; revised 28 July 2003; accepted 21 August 2003; published 22 November 2003.

[1] The acceleration of coronal mass ejections (CMEs) is examined focusing on three specific questions raised by observations: (1) what determines the height beyond which a CME exhibits no rapid acceleration, (2) why is the main acceleration of CMEs typically limited to below 2–3 solar radii, and (3) are distinct mechanisms required to explain the apparent bimodal distribution of speed-height profiles. Using a theoretical model of CMEs based on a three-dimensional (3-D) magnetic flux rope, it is shown that the acceleration of CMEs exhibits a universal scaling law characterized by the critical height $Z_* = S_f/2$ such that maximum acceleration is attained shortly after height Z of the flux-rope apex exceeds Z_*, where S_f is the footpoint separation distance. Theoretical analysis and observed CME dynamics show two distinct phases of acceleration: the "main" and "residual" acceleration phases. The main acceleration phase occurs for apex height $Z \leq Z_m$, where Z_m is found to be $\simeq 3\ Z_*$, and the residual acceleration phase corresponds to $Z > Z_m$. Thus the observed acceleration profile can be directly related to S_f. These results are explained in terms of the 3-D geometry of a flux rope, its inductive properties, and the Lorentz self-force. We have also constructed ensembles of flux-rope profiles corresponding to varying amounts and durations of poloidal flux injection. We find that the resulting distribution of model speed-height profiles is similar to that observed if an upper limit on the amount of injected flux is imposed. One mechanism is sufficient to account for the observed properties and distribution of CME acceleration. The theory is quantitatively tested against observed CMEs. *INDEX TERMS:* 7513 Solar Physics, Astrophysics, and Astronomy: Coronal mass ejections; 7827 Space Plasma Physics: Kinetic and MHD theory; 2111 Interplanetary Physics: Ejecta, driver gases, and magnetic clouds; 7524 Solar Physics, Astrophysics, and Astronomy: Magnetic fields; 7509 Solar Physics, Astrophysics, and Astronomy: Corona; *KEYWORDS:* CME acceleration, CME initiation, scaling law, flux rope eruption, solar and stellar eruptions

Citation: Chen, J., and J. Krall, Acceleration of coronal mass ejections, *J. Geophys. Res.*, *108*(A11), 1410, doi:10.1029/2003JA009849, 2003.

1. Introduction

[2] A coronal mass ejection (CME) represents an estimated 10^{14}–10^{16} g of material ejected from the Sun at a projected speed of ~100–2000 km s^{-1} [*Gosling et al.*, 1976; *Howard et al.*, 1985; *St. Cyr et al.*, 1999]. Observations have shown that the bulk of the acceleration occurs near the Sun. *MacQueen and Fisher* [1983] examined CMEs observed by the Mauna Loa Mark III K-coronameter (MK3) and the Skylab coronagraph, having Sun-centered fields of view (FOVs) of 1.2–2.4 and 1.5–6 solar radii ($R_\odot$), respectively. The data from this sample, 12 MK3 and 10 Skylab events, indicate that the main acceleration of most CMEs occurs below 2–3 $R_\odot$. A larger sample of 246 CMEs observed by MK3 and Solar Maximum Mission (SMM) (FOV 1.7–6 $R_\odot$) shows that CMEs on the average gain the bulk of their speed before leaving the MK3 FOV [*St. Cyr et al.*, 1999]. *Vršnak* [2001] found that acceleration maxima typically occur below ~4 $R_\odot$.

[3] Coronal mass ejections often occur in association with flares and prominence eruptions, with flare-associated CMEs attaining faster speeds than those associated with eruptive prominences [e.g., *Gosling et al.*, 1976]. More broadly, active region-associated CMEs, of which flare-associated CMEs would be a subset, tend to be faster than solitary prominence-associated ones [*St. Cyr et al.*, 1999].

[4] Examining the kinematics of CMEs detected by MK3, *MacQueen and Fisher* [1983] discerned two kinds of speed-height profiles in the plane of the sky: flare-associated CMEs tend to show little or no acceleration beyond the edge of the occulting disk (1.2 $R_\odot$), while eruptive prominence-associated CMEs tend to show detectable acceleration. The acceleration of the former was characterized as "impulsive." *St. Cyr et al.* [1999] found that in the combined MK3-SMM data, active region-associated CMEs tend to show larger average acceleration than solitary prominence-associated CMEs. *Sheeley* [1999] examined the distribution of height-time profiles of a sample of CMEs observed by the Large Angle and Spectrometric Coronagraph (LASCO) [*Brueckner et al.*, 1995] on the Solar and Heliospheric Observatory (SOHO) satellite and found that it consists of those that can be approximated by linear

(constant-speed) fits and those that can be described by quadratic (constant-acceleration) fits within the LASCO C2-C3 FOV, which is 2–32 $R_\odot$ (2–6 $R_\odot$ and 4–32 $R_\odot$, respectively). The latter population (''gradual'' CMEs) is significantly slower on the average than the former (''impulsive'' CMEs), and none in this sample shows rapid acceleration. Thus statistical analyses of CME motion point to speed-height distributions that are apparently bimodal in different height ranges (MK3, SMM, or C2-C3). Such a distribution originally led *MacQueen and Fisher* [1983] to suggest that there exist two classes of CMEs driven by fundamentally different acceleration mechanisms. This suggestion was supported by *Sheeley et al.* [1999] and *Moon et al.* [2002] based on LASCO C2-C3 CME data.

[5] The fact that CMEs typically undergo most of their acceleration below $\simeq$3 $R_\odot$ raises a number of fundamental questions: (1) what determines the height beyond which a CME exhibits no rapid acceleration, (2) why is the main acceleration of CMEs typically limited to below 2–3 solar radii, and (3) are distinct mechanisms required to explain the apparent bimodal distribution of speed-height profiles. The purpose of the present paper is to provide quantitative and physics-based answers to these questions.

[6] To answer these questions, it is essential to examine in detail the driving forces from the onset. It is widely accepted that the forces causing CME eruptions are magnetic. However, the magnetic field structure that underlies a CME and the precise nature of the forces acting on such a structure are still a matter of debate. In the present paper, we use the flux-rope model of *Chen* [1989] to study the forces acting on CMEs. The theory posits that a CME is topologically a 3-D magnetic flux rope and determines the macroscopic Lorentz force, pressure gradient force, momentum coupling to the ambient magnetized plasma, and gravitational force acting on the flux rope [*Chen and Garren*, 1993; *Chen*, 1996]. The model has been tested against numerous LASCO CMEs, and the results have been demonstrated to be in good agreement with observed CME dynamics in the corona and magnetic cloud properties in interplanetary space [*Chen et al.*, 1997, 2000; *Wood et al.*, 1999; *Krall et al.*, 2001]. A number of other CMEs have been similarly interpreted as erupting flux ropes [*Dere et al.*, 1999; *Plunkett et al.*, 2000; *Wu et al.*, 1999]. Indeed, *Krall et al.* [2001] have shown that flux-rope CMEs constitute an identifiable subclass of CMEs. Quantitatively, the comparisons extend down to LASCO C1 (FOV 1.1–3 $R_\odot$) [*Wood et al.*, 1999] and MK3 [*Chen et al.*, 2000] heights and are constrained by the observed height and width, two orthogonal dimensions, of CMEs. Thus the model equations can correctly describe the forces acting on a CME from the early phases.

[7] In section 2, we examine the acceleration of three different flux-rope CMEs observed by C1, C2, and C3. We then discuss the geometry and inductance of a flux rope that determine the accelerating forces (section 3). We identify two principal phases of acceleration, the ''main'' and ''residual'' phases, distinguished by how the driving forces operate. It is shown that there exist specific temporal and spatial scales governing the acceleration process during the respective phases. These results provide the answers to questions 1 and 2 posed earlier. In section 4, we test the theoretical predictions against observed CME acceleration profiles. In section 5, we construct a synthetic distribution of CME speed-height curves using the model and show that one mechanism is sufficient to reproduce and explain the observed distributions, answering question 3. Section 6 provides a discussion of the observable properties of acceleration that can serve as diagnostics and discriminators of physical mechanism(s) of CMEs. The physical differences and similarities between a number of models are discussed. The conclusions of the paper are summarized in section 7.

2. Properties of CME Acceleration

[8] Although observations indicate that CMEs undergo most of their acceleration early in the eruption process, the onset and the initial acceleration are often not well observed. This is because many CMEs erupt on the disk and even when they occur on the limb, the initial phase is usually blocked by the occulting disk of the observing coronagraph. Nevertheless, some limb CMEs have been observed by C1 or MK3 accompanied by observations of the associated surface activities obtained by the SOHO Extreme Ultraviolet Imaging Telescope (EIT) [e.g., *Dere et al.*, 1997, 1999; *Wood et al.*, 1999; *Chen et al.*, 2000; *Plunkett et al.*, 2000; *Zhang et al.*, 2001]. In particular, *Wood et al.* [1999] and *Zhang et al.* [2001] examined height-time data for several fast and slow CMEs imaged by EIT and LASCO C1, C2, and C3. These CMEs were limb events, and their motions were measured from the initial eruptions to the outer edge of the C3 FOV. *Chen et al.* [2000] analyzed and modeled a fast CME observed by EIT, MK3, C2, and C3. Regardless of their speeds, these CMEs have prominent peaks in their acceleration profiles at C1/MK3 heights and exhibit much weaker acceleration, positive or negative, in the C2-C3 FOV. Less frequently, CMEs exhibit acceleration peaks at 3–4 $R_\odot$ [e.g., *Plunkett et al.*, 2000; *Srivastava et al.*, 2000] with only slow acceleration at C1/MK3 heights. Based on representative CMEs, *Vršnak* [2001] concluded that CME acceleration maxima typically occur below $\simeq$4 $R_\odot$. The acceleration of CMEs, when observed from the onset, is generally peaked low in the corona and cannot be approximated by constant speed or constant acceleration. We will illustrate these features using three well-observed examples and use them to test theoretical results in section 4.

2.1. Profiles of CME Acceleration

[9] Figures 1 and 2show the data (diamonds) for the 23 February 1997 and 30 April 1997 CMEs. These CMEs were limb events and were observed by EIT, C1, C2, and C3 so that their height-time data give a good description of the initial acceleration as well as the subsequent expansion. They have both been identified as flux-rope CMEs and theoretically modeled as such by *Wood et al.* [1999]. Similar CME acceleration profiles have been reported by *Zhang et al.* [2001].

[10] For each event, the top panel shows the measured height of the leading edge from Sun center. The second panel shows the speed determined from successive pairs of height data points. The calculated value is assigned to the midpoint of each pair. Similarly, the acceleration of the leading edge (third panel) is calculated using sucessive pairs of speed values. The data points and the associated error bars are those of *Wood et al.* [1999]. (The exception is the fourth acceler-

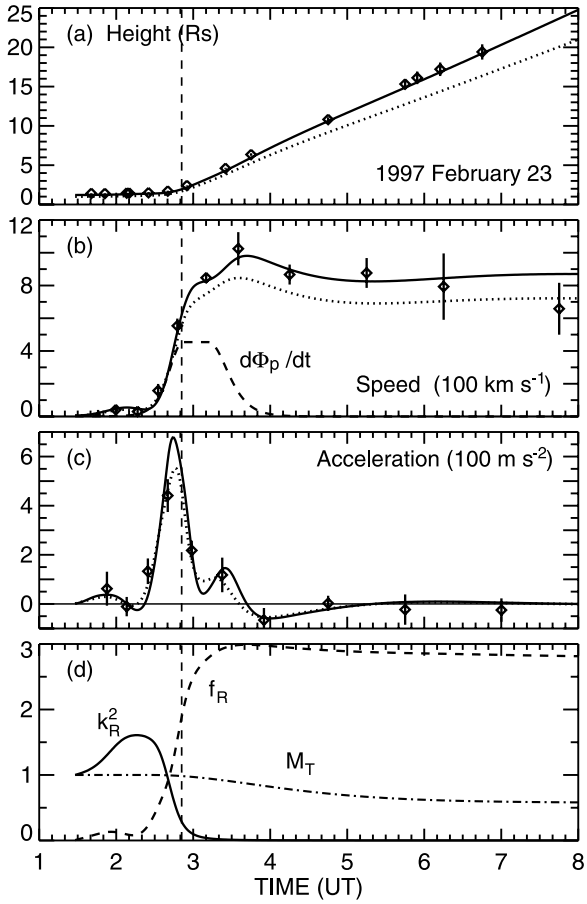

Figure 1. Dynamics of 23 February 1997 CME observed by LASCO C1, C2, and C3. The data points (diamonds) and the error bars are from *Wood et al.* [1999]. The curves are theoretical results providing the best agreement: the solid curves refer to the leading edge (LE) and the dotted curves refer to the centroid. The vertical dashed line in each panel corresponds to the time when the LE reached 2 $R_\odot$ from Sun center. (a) Height. (b) Speed derived from the height-time data. The poloidal flux inection profile ($d\Phi_p/dt$) is shown (dashed curve) in units of 2×10^{18} Mx s^{-1} with the peak value at 9.1×10^{18} Mx s^{-1}. The leading edge attains a maximum speed of $\sim$1000 km s^{-1}. (c) Acceleration in units of 100 m s^{-1}. The main acceleration phase ends at $\simeq$0300 UT. (d) k_R^2 (solid) defined by equation (12b) and normalized to the initial value; f_R (dashed) defined by equation (8); $\mathcal{M}_T$ (dash-dot) is the total mass of the flux rope, consisting of the cavity mass (constant) and prominence mass (decreasing to 15% of the initial value).

ation point for the 30 April event. In the work of Wood et al., some data points closely spaced in time were omitted to avoid large fluctuations. No data points were omitted in calculating the speed and acceleration in Figure 2.) The data points for the centroid of the bright rim were published by Wood et al. for each event and are not shown here. The various curves in the figures are theoretically computed quantities from the "best-fit" solutions and will be discussed later. The dashed vertical line in each panel denotes where the observed leading edge reached the inner edge of the C2 FOV at 2 $R_\odot$.

[11] The leading edge of the 23 February 1997 CME attained a maximum speed somewhat greater than 1000 km s^{-1} at about 0330 UT (Figure 1). The acceleration was $\sim$450 m s^{-2} at $\sim$0240 UT when the leading edge was at $\sim$1.75 $R_\odot$, rapidly decreasing afterwards and followed by slow deceleration. This mass ejection was accompanied by an eruptive prominence and a B7 GOES X-ray flare. Note that the maximum in the acceleration, or equivalently the maximum in the driving force, occurs before the speed reaches its maximum because speed is acceleration integrated in time. This means that the determination of the onset time of an event based on height-time measurement can be in error if the entire acceleration profile is not available.

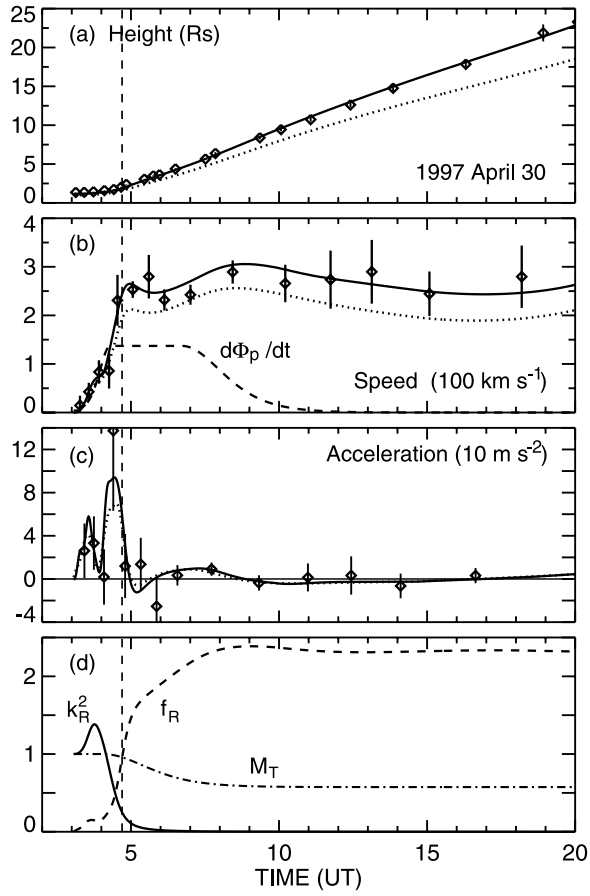

Figure 2. Dynamics of 30 April 1997 limb CME observed by LASCO C1, C2, and C3. The format is the same as that of Figure 1, with the vertical dashed line corresponding to the inner edge of the C2 FOV. (a) Height of the LE. (b) Speed and $d\Phi_p/dt$ (dashed) in units of 6×10^{17} Mx s^{-1}. The LE motion is consistent with nearly constant speed at 250–300 km s^{-1} in the C2-C3 FOV, but a small-amplitude oscillation is evident. The maximum poloidal flux injection rate is 8.2×10^{17} Mx s^{-1}. (c) Acceleration in units of 10 m s^{-1}. The main acceleration ends at $\simeq$0500 UT. (d) k_R^2 (solid) normalized to the initial value; f_R (dashed); $\mathcal{M}_T$ (dash-dot) is the total mass of the flux rope.

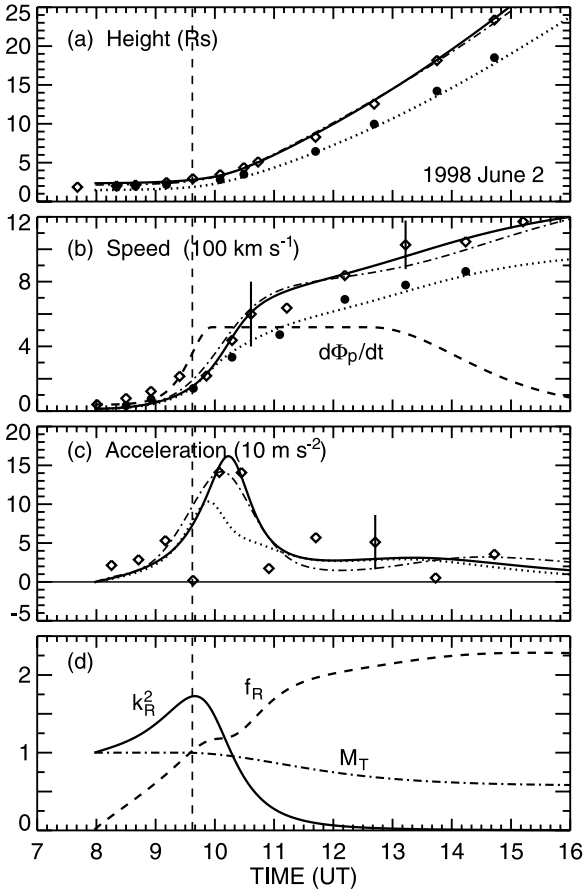

Figure 3. CME of 2 June 1998. LASCO C1, C2, and C3 data: open diamonds (leading edge) and solid circles (centroid). Representative error bars are shown. The solid and dotted curves in Figures 3a–3c show the solution for $S_f = 1.8\ R_\odot = 1.26 \times 10^6$ km, with the dash-dot curves corresponding to $S_f = 1.5\ R_\odot = 1.05 \times 10^6$ km. (a) Height. (b) Speed and $d\Phi_p/dt$ (dashed, in units of 5×10^{17} Mx s^{-1}). The maximum injection rate is 2.5×10^{18} Mx s^{-1}. (c) Acceleration in 10 m s^{-1}. The dotted curve is the centroid acceleration. (d) k_R^2 (solid), f_R (dashed), $\mathcal{M}_T$ (dash-dot) as in Figures 1 and 2.

[12] The 30 April 1997 CME exhibited a slower, nearly constant speed of ~275 km s^{-1} in the C2-C3 FOV (Figure 2b). Within the C1 FOV, the leading edge appeared to undergo momentary deceleration, followed by a sharp reacceleration. Still, as in the much faster 23 February CME, the peak acceleration (~140 m s^{-2}) occurred within the C1 FOV, with the acceleration declining to nearly zero in the C2 FOV. There was no significant (exceeding A class) GOES X-ray event or an observed prominence eruption.

[13] Figure 3 shows the C1-C2-C3 data (open diamonds) for the leading-edge motion of the 2 June 1998 CME, a study of which has been previously published by *Plunkett et al.* [2000]. Representative error bars are shown. The measured position and speed of the centroid of the bright rim are also shown (solid circles), but the acceleration data points are not shown for clarity of the figure. The CME slowly expanded at C1 heights, appearing as a "streamer blowout" [*Howard et al.*, 1985] in the C2 FOV. Figure 3c shows that the most significant acceleration (~150 m s^{-2}) occurred at ~1000 UT and ~3.5 $R_\odot$. The peak acceleration period has a width of ~1.5 hours at half maximum. By about 1100 UT, the acceleration was already significantly less than the maximum value. The C3 data for this event are consistent with a constant acceleration of 30–50 m s^{-2}. The 21–22 June 1998 CME [*Srivastava et al.*, 2000] is similar to this event in that the acceleration peaked in the 3–4 $R_\odot$ range, but the maximum acceleration was only ~20 m s^{-2}.

2.2. Observed Distribution of CME Speed

[14] In Figure 4, we show the measured speed-height profiles of 16 LASCO (C2-C3) CMEs, where speed and height refer to the leading edges of CMEs projected onto the plane of the sky. Each curve is generated by taking differences of successive height data points to obtain the speed data which are then smoothed numerically. (Because no polynomial fitting is used, the curves show variations in speed for each event.) The plot is similar to those of *MacQueen and Fisher* [1983, Figures 3 and 5] and *Sheeley* [1999, Figure 10] in that it is possible to discern two populations: one with essentially constant speeds and the other with "gradual" accelerations. One difference between Figure 4 and *Sheeley*'s [1999] figure is that the latter does not include events such as the 2 June 1998 event (curve 3) that undergo relatively fast acceleration at C2-C3 heights or those that show noticeable deceleration (curve 1).

[15] A significant difference between Figure 4 and the previous speed-height plots is that the events in Figure 4 are limited to those identified as flux-rope CMEs based on both the morphological features and agreement with theoretically predicted dynamics of magnetic flux ropes. For agreement between observation and theory, we demand that the calculated flux-rope dynamics match the observed height and speed profiles in the radial as well as the transverse directions. This is a more stringent demand than fitting only the radial motion of the leading edge. The events in Figure 4 satisfy this theory-observation agreement requirement. The CMEs included here are the two events shown in Figures 1 and 2 (curves 1 and 2), the 2 June 1998 CME (curve 3), the 11 flux-rope CMEs studied by *Krall et al.* [2001], the 13 April 1997 event [*Chen et al.*, 1997], and the fast CME of 9 September 1997 [*Chen et al.*, 2000].

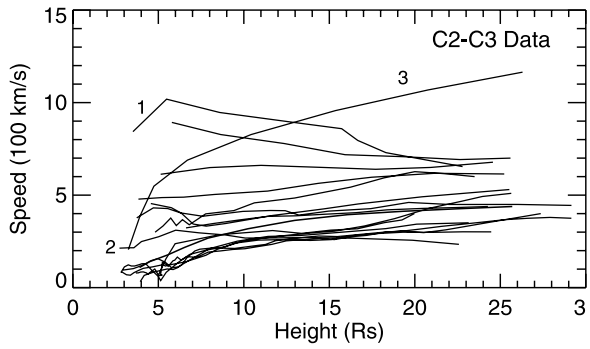

Figure 4. Speed versus height data for 16 flux-rope CMEs observed by LASCO C2 and C3. Curves 1–3 correspond to the 23 February 1997, 30 April 1997, and 2 June 1998 CMEs, respectively. These events are shown in Figures 1–3.

[16] The speed-height curves in Figure 4 and previously published plots do not account for the projection effects. Nevertheless, the data from various instruments seem to suggest the existence of similar distributions even when the sample is restricted to clearly identifiable flux-rope CMEs.

[17] Except for the CME of 1998 June 2 (curve 3), the maximum sustained acceleration averaged over the C2-C3 FOV in this sample is $\sim$10 m s^{-2}, which is substantially smaller, by more than an order of magnitude, than the peak value for the 23 February CME. In previous studies, the accelerations of prominence-associated CMEs have been shown to have a median value of $\sim$50 m s^{-2} averaged over the MK3-SMM FOV, while the active region-associated CMEs have a median acceleration of $\sim$160 m s^{-2} [*St. Cyr et al.*, 1999], with higher values (>1000 m s^{-2}) inferred in some events [e.g., *St. Cyr et al.*, 1999; *Zhang et al.*, 2001; *Vršnak*, 2001; *Alexander et al.*, 2002; *Gallagher et al.*, 2003].

[18] In the previous characterizations of CME acceleration, the focus is on the presence or absence of significant acceleration and the average value of acceleration within some range of heights. In our discussion, we take a different approach: we focus on features in an acceleration profile in its entirety, from the onset to the outer edge of observability. In the next section, we will examine the physical forces that determine the spatial and temporal scales characterizing certain observable features in the acceleration of flux-rope CMEs.

3. Physics of Erupting Flux Ropes

[19] For the acceleration of flux-rope CMEs, the 3-D geometry and the Lorentz self-force acting on an expanding flux rope each play a key role in determining the forces. They have been previously discussed in general terms [*Chen*, 1989, 1996], but here, we isolate specific aspects to show how they are manifested in the observed CME dynamics. In particular we will focus on the fixed footpoint separation distance and the inductance of the flux rope. The theory uses ideal magnetohydrodynamics (MHD) with zero resistive dissipation.

3.1. Magnetic Flux Ropes

[20] A flux rope is a 3-D plasma structure consisting of a current channel $\mathbf{J}(\mathbf{x})$ and the magnetic field $\mathbf{B}(\mathbf{x})$ given by $\mathbf{J} = (c/4\pi)\nabla \times \mathbf{B}$. Figure 5 shows a schematic with the flux rope viewed side-on. The current is localized to a channel of major radius R and minor radius a. That is, $|\mathbf{J}(r \leq a)| \gg |\mathbf{J}(r > a)|$. For simplicity, we take $\mathbf{J} = 0$ for $r > a$. Inside the current channel ($r < a$), $\mathbf{J}$ has toroidal, $J_t(r)$, and poloidal, $J_p(r)$, components, producing the poloidal, $B_p(r)$, and toroidal, $B_t(r)$, fields, respectively. For $r < a$, magnetic field "lines" are helical. A representative helical line inside the current channel is illustrated. For $r > a$, $J_t = 0$, and the field is purely poloidal. If the total toroidal current is denoted by $I_t(t) \equiv 2\pi \int r J_t(r, t)\, dr$, we have $B_p(r) = 2I_t/cr$ for $r > a$ independently of the form of $J_t(r)$ for $r \leq a$. By "flux rope," we refer to the current channel plus the magnetic field produced by the current, including the poloidal field outside the current channel. The footpoints are separated by S_f and are assumed to be stationary. (Note that $S_0 \equiv S_f/2$ was used in a number of earlier papers.)

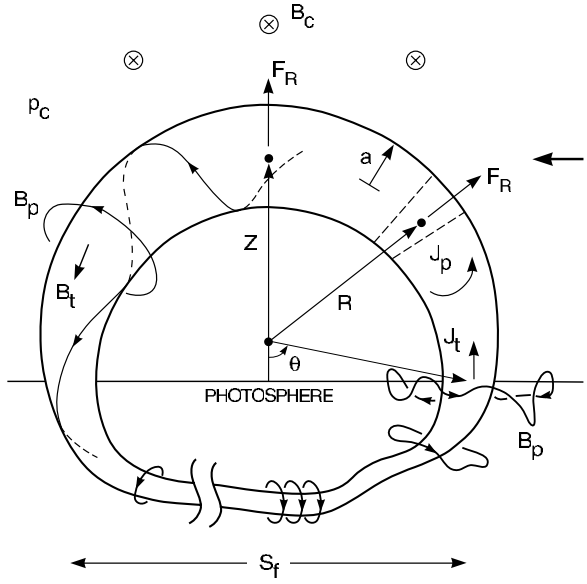

Figure 5. Schematic of a magnetic flux rope. Toroidal (locally axial) and poloidal (locally azimuthal) components of the current **J** and magnetic field **B** are shown. The flux rope consists of the current channel of radius a and the self ("private") magnetic field. Z refers to the centroid of the apex. S_f is the distance between the fixed footpoints at the base of the corona. The flux rope is viewed side-on with the plane of the flux rope in the plane of the paper. The short arrow in the upper right-hand corner indicates the end-on viewing perspective. Adapted from *Chen* [1989].

[21] A flux rope has average density $\overline{n}$ and pressure $\overline{p}$ embedded in an ambient corona defined by density $n_c(z)$ and pressure $p_c(z)$, with the overlying coronal magnetic field $B_c(z)$ indicated by B_c in Figure 5. We use z to denote the vertical coordinate and $Z(t)$ to denote the height of the centroid of the apex (or simply the "apex") of the flux rope measured from the surface. We will use T to denote observational time in UT and t to denote time in model calculations. In our comparisons with coronagraph images, we use $2a(t)$ as a proxy for the radius of the bright rim when the flux rope is viewed end-on [*Chen et al.*, 1997]. This viewing perspective is indicated by the short arrow on the right in Figure 5. Thus the leading edge of the apex is at $Z(t) + 2a(t)$, and the width of the bright rim is $4a(t)$ (viewed end-on) or $2R + 4a$ (viewed side-on). This ad hoc definition of the leading edge and width is motivated by the fact that B_p decreases to about half the value of $B_{pa} \equiv B_p(r = a)$ at $r = 2a$, at which point B_p may be comparable to the ambient coronal field. We have consistently used this definition in our previous comparisons, obtaining good agreement with both the leading edge height and width of CMEs [*Chen et al.*, 1997, 2000; *Wood et al.*, 1999; *Krall et al.*, 2001]. Noting that $Z(t)$ and $a(t)$ are two independent and orthogonal degrees of freedom, the agreement is stronger than that with only one or the other quantity.

[22] The footpoints of the flux rope at the base of the corona have minor radius a_f and separation distance S_f. For simplicity, the major radius R is taken to be uniform, but the minor radius a is variable: minimum at the footpoints with $a = a_f$ and monotonically increasing to a maximum

value $a = a_a$ at the apex. Here, $Z(t)$, $R(t)$, and $a(t)$ are functions of time while S_f and a_f remain constant. The model corona, solar wind (SW), and $B_c(z)$ are specified in the same way as in the work of *Chen* [1996]. The SW speed, V_{sw}, is ramped up to 400 km s^{-1} (slow wind) or 600 km s^{-1} (fast wind) at $\sim 20\ R_\odot$.

[23] The model only treats the dynamics of the flux rope in the corona, but the flux rope is taken to be part of a larger current system embedded below the photosphere. The total toroidal current $I_t(t)$ is constant along the flux rope in the corona due to continuity of electric current ($\nabla \cdot \mathbf{J} = 0$), but the precise subphotospheric current distribution does not enter the model. We implicitly assume that the magnetic energy of the entire flux system is ultimately generated by some dynamo processes in the convection zone. The energy in excess of the local equilibrium propagates up along the subphotospsheric flux rope at $V \leq V_M$, the local magnetosonic speed [*Chen*, 2001]. Thus the eruption is driven by nonzero Poynting flux P_n through the solar surface associated with increasing the poloidal flux. Because V_M depends on the local magnetic field, mass density, and plasma pressure, the poloidal magnetic field at the photosphere (plasma $\beta \gg 1$) should be highly nonuniform. In the low-β ($\beta < 1$) corona, however, because of higher Alfvén speed, magnetic field is expected to be more coherent even under dynamic conditions. The expected nonuniform subphotospheric poloidal field is represented by wavy poloidal field lines in Figure 5. The transition layer between the photosphere and the corona is not treated.

3.2. Inductance of a Flux Rope

[24] As a flux rope expands, the electric current and therefore the magnetic field of the flux rope evolve because of the inductive properties of the flux rope. The inductance increases as the current-carrying structure expands. Thus the geometrical size of an expanding flux rope plays a determining role in the acceleration process.

[25] The inductance of a flux rope arises as a geometrical factor relating the magnetic energy of the flux rope to its current. The poloidal magnetic energy of the flux rope associated with B_p above the photosphere is

$$U_p = \frac{1}{8\pi}\int B_p^2 d^3\mathbf{x} \equiv \frac{1}{2}LI_t^2, \tag{1}$$

where the last expression serves to define the self inductance L of the current-carrying plasma system [*Landau et al.*, 1984]. Maxwell's equations also lead to

$$\Phi_p = cLI_t. \tag{2}$$

Here, Φ_p is the magnetic flux enclosed by the current loop above the photosphere, defined by $\Phi_p \equiv \oint B_p d\sigma_p$, where $d\sigma_p$ is a surface area element in the plane of the flux rope, and $\oint$ denotes integration over the surface enclosed by the toroidal axis of the current loop and a path connecting the two footpoints of the flux rope. The toroidal flux Φ_t is given by $\Phi_t = \pi \overline{B}_t a^2$, where $\overline{B}_t$ is the toroidal field averaged over the minor cross-section ($r \leq a$). We assume ideal MHD with no resistivity so that Φ_t is conserved. The poloidal flux, Φ_p, is also conserved except for a prescribed amount that is added to or "injected" into the system.

[26] For uniform major radius R with the minor radius a monotonically increasing from the value a_f at the footpoints to a_a at the apex, the inductance is approximated by [*Chen and Garren*, 1993; *Garren and Chen*, 1994]

$$L = \frac{4\pi\Theta R}{c^2}\mathcal{L}(R, a_a, a_f), \tag{3a}$$

where

$$\mathcal{L}(R, a_a, a_f) \equiv \frac{1}{2}\left[\ln\left(\frac{8R}{a_f}\right) + \ln\left(\frac{8R}{a_a}\right)\right] - 2 + \frac{\xi_i}{2}, \tag{3b}$$

and Θ is the fractional angular extent of the flux rope such that $2\pi\Theta R$ is the arc length of the loop from footpoint to footpoint. Here, $\Theta = 1 - \theta/\pi$ for $Z \geq S_f/2$ and $\Theta = \theta/\pi$ for $Z < S_f/2$, with θ shown for $Z \geq S_f/2$ in Figure 5. In using equation (3b), we have assumed that the form of $J_t(r)$ is the same as a varies along the flux rope.

[27] The detailed form of $\mathbf{J}(r)$ enters the inductance only through the internal inductance ξ_i, which gives the magnetic energy of the poloidal field inside the current channel via the expression $U_{pi} \equiv (1/2)L_i I_t^2$, where $L_i \equiv (2\pi\Theta R/c^2)\xi_i$. For typical flux ropes, we find $\xi_i/2 \simeq 1/2$, and the form of $\mathbf{J}(r)$ has relatively small influences on the flux rope dynamics and energy budget. For concreteness, we use a $\mathbf{J}(r)$ profile that vanishes smoothly at $r = a$, for which $\xi_i = 1.2$ [*Chen*, 1996]. For such profiles, the toroidal magnetic field $B_t(r)$ is maximum at $r = 0$, with $B_t(r = 0) > \overline{B}_t$.

[28] The energy associated with the external inductance $L_e \equiv L - L_i$ is

$$U_{pe} = \frac{1}{2}L_e I_t^2, \tag{4a}$$

where $U_p = U_{pe} + U_{pi}$. Because $\xi_i \sim 1$, we have $L_e > L_i$ from (3b) so that

$$U_{pe} > U_{pi}. \tag{4b}$$

Thus the energy of eruption predominantly resides in the poloidal field outside the current channel ($r \geq a$), represented by the wavy curves marked B_p in Figure 5.

[29] For the initial flux rope, we assume $a_a = a_f$. Then, $\ln(8R/a_a) = \ln(8R/a_f)$ at $t = 0$, and we have $\mathcal{L} \sim \ln(8R/a_f)$. After the eruption, a_a becomes much greater than a_f (i.e., $R/a_f \gg R/a_a$) so that $\mathcal{L} \simeq (1/2)\ln(8R/a_f)$. Thus equation (3a) has the scaling

$$L \propto R\ln\left(\frac{8R}{a_f}\right). \tag{5}$$

[30] This dependence of L arises from the monotonic increase of a from the small footpoint value a_f to the apex value $a_a \gg a_f$. It is not sensitive to the value of a_a or the precise way a varies along the flux rope because L is dominated by the $\ln(8R/a_f)$ term. Equation (3) can be derived if one assumes $a(\theta) = a_f \exp[s(\theta - \theta_f)]$, where $s > 0$ is a constant and $\theta_f \leq \theta \leq \pi$ ($0 \leq \theta \leq \theta_f$) if $Z > S_f/2$ ($Z < S_f/2$). Alternatively, one may assume that a increases linearly from a_f to a_a [*Krall et al.*, 2000]. In this case, if we

write $a_a(t) = \nu(t)a_f$, where $\nu \geq 1$, the inductance takes on the form

$$L = \frac{4\pi\Theta R}{c^2}(\mathcal{L} + \Delta), \tag{6a}$$

where

$$\Delta(t) \equiv 1 - \frac{(\nu+1)}{2(\nu-1)}\ln(\nu). \tag{6b}$$

Because $\nu \geq 1$, we have $\Delta \leq 0$. The additive quantity Δ depends only on the ratio $\nu = a_a/a_f$. For the initial flux rope, we set $a = a_f$ so that $\nu = 1$ and $\Delta = 0$. As the flux rope expands away from the Sun, $\nu(t)$ increases. For $\nu \gg 1$, $\Delta \simeq 1 - (1/2)\ln(\nu)$. For a typical flux-rope CME at the outer edge of the C3 FOV (30 $R_\odot$), $\nu \simeq 20$, and $|\Delta/\mathcal{L}| \simeq 0.2$. At 1 AU, where a_a corresponds to half-width of a magnetic cloud, we have $a_a/a_f \sim 200$, and the fractional difference slightly increases to $|\Delta/\mathcal{L}| \simeq 0.3$.

[31] Physically, as the flux rope erupts, the $\ln(8R/a_f)$ term increasingly dominates $\ln(8R/a_a)$ in equation (3). Because the poloidal energy is $U_p = LI_t^2/2$, an increasing fraction of the poloidal energy, $\ln(8R/a_f)/[\ln(8R/a_f) + \ln(8R/a_a)]$, becomes associated with the legs of the flux rope as a_a/a_f increases. This means that the apex motion, which is governed by $\ln(8R/a_a)$, cannot access the poloidal energy of the entire flux rope. Effectively, the apex motion is energetically decoupled from the legs of the flux rope as the expansion continues.

[32] That L scales with $\ln(R/a_f)$ rather than $\ln(R/a_a)$ is important. Because $R/a_a \sim$ const [*Chen et al.*, 1997, 2000; *Krall et al.*, 2001] for flux-rope CMEs while R/a_f increases, the time-dependence of $R\ln(8R/a_f)$ differs from that of $R\ln(8R/a_a)$. For example, the inductance of a Sun-encircling 2.5-D model flux rope that matches an observed CME at a given time would evolve according to $R\ln(8R/a_a)$, diverging from the dynamics of the 3-D flux rope with constant S_f and a_f.

3.3. Forces Acting on a Flux Rope

[33] In MHD, the force acting on a unit volume with density ρ in gravitational potential φ is

$$\mathbf{f} = (1/c)\mathbf{J} \times \mathbf{B} - \nabla p + \rho\nabla\varphi.$$

Integration of $\mathbf{f}$ over a toroidal section gives the major radial force per unit length of the flux rope. (One toroidal section is shown as a wedge in Figure 5.) The contribution from $\mathbf{J} \times \mathbf{B}/c$ and ∇p is approximately [*Chen*, 1989]

$$F_R = \frac{I_t^2}{c^2 R} f_R, \tag{7a}$$

where we have defined

$$f_R(t) \equiv \ln\left(\frac{8R}{a}\right) + \frac{1}{2}\beta_p - \frac{1}{2}\frac{\overline{B}_t^2}{B_{pa}^2} + 2\left(\frac{R}{a}\right)\frac{B_c(Z)}{B_{pa}} - 1 + \frac{\xi_i}{2}. \tag{7b}$$

Here, $B_{pa} \equiv B_p(r = a) = 2I_t/ca$, $\beta_p \equiv 8\pi(\overline{p} - p_c)/B_{pa}^2$, $\overline{p}$ and $\overline{B}_t$ are the average pressure and toroidal field inside the current channel ($r \leq a$), and $p_c(z)$ is the ambient ($r > a$) coronal pressure. Here, the β_p term is the toroidal force per unit length arising from the pressure gradient between the flux-rope and ambient coronal pressures, and all other terms arise from the Lorentz self-force, the interaction between the current $\mathbf{J}$ and self or "private" field $\mathbf{B}$ of the flux rope determined by $\mathbf{J} = (c/4\pi)\nabla \times \mathbf{B}$, and ∇p except that $B_c(Z)/B_{pa}$ is the interaction of I_t with the ambient B_c. The self-force arises from the toroidicity of the flux rope, vanishing in the limit of $R \to \infty$ for any finite a.

[34] The major radial force F_R is directed outward for $F_R > 0$, as illustrated in Figure 5. The motion of the apex, i.e., its center of mass, is described by the equation

$$M\frac{d^2Z}{dt^2} = \frac{I_t^2}{c^2 R} f_R + F_g + F_d, \tag{8}$$

where $M = \pi a^2\bar{\rho}$ is the mass per unit length of the flux rope, $\bar{\rho} \equiv m_i\overline{n}$ is the average mass density inside the flux rope, and Z is the height of the centroid of the apex. The terms F_g and F_d arise, respectively, from gravity and momentum coupling (drag) between the flux rope and the ambient corona and have been previously discussed. The gravity term, including the prominence mass, is usually much smaller than F_R. Although gravity does not dominate CME dynamics, it does affect the magnetic energy of the initial flux rope and the resulting flux rope at 1 AU and beyond [*Chen*, 1996]. In the arcade geometry, including the effects of gravity has also been shown to increase the stored magnetic energy [*Wolfson and Saran*, 1998]. The present model includes the minor radial dynamics d^2a/dt^2, but they are not explicitly discussed here.

[35] The factor (I_t^2/c^2R) in equation (8) can be written in equivalent form in terms of Φ_p and L. Using equations (2) and (3), the major radial acceleration takes on the form

$$\frac{d^2Z}{dt^2} = \left(\frac{\Phi_p^2}{2\pi\mathcal{M}_T\Theta R^2\mathcal{L}^2}\right) f_R + f_g + f_d, \tag{9}$$

where $f_g(t) \equiv F_g/M$, $f_d(t) \equiv F_d/M$, $\mathcal{M}_T(t) \equiv 2\pi\Theta RM$ is the total mass of the flux rope, and $\mathcal{L}$ is defined in equation (3b). This form is instructive because it shows how the poloidal flux $\Phi_p(t)$ and the inductance $L(t) \propto R\mathcal{L}$ enter the force equation and will be the basis of the discussion in the remainder of the paper.

[36] The constraint that the footpoint separation S_f be fixed and the geometrical simplification of a uniform major radius R relate apex height Z to R at any time by

$$R = \frac{\left(Z^2 + S_f^2/4\right)}{2Z}. \tag{10}$$

Equation (9) along with equations (2), (5), and (10) are the basic equations that determine the major radial acceleration.

[37] We digress here and discuss a point of some confusion concerning the equations given above, i.e., the relationship between these equations and the usual MHD equations. The more familiar form of MHD equations are expressed as partial differential equations. However, because of nonlocality of magnetic field, which is evident in Biot-Savart law, the MHD equations are actually integro-

differential equations. The above equations are the integral representation of the usual MHD equations assuming an a priori geometry, i.e., a section of a torus with fixed footpoints. This enables one to use the equivalent integral form of Maxwell's equations in combination with the fluid equations and express the equations of motion in the form used here. This approximation allows us to analytically capture certain essential nonlocal 3-D effects, such as the toroidal hoop force (equation (7)), the inductance of the toroidal plasma structure (equation (3a)) with fixed footpoints (equation (10)), and the relationship between the toroidal current and poloidal flux above the photosphere (equation (2)). Mathematically, the nonlocality and 3-D dynamics are embodied in equation (9) via equations (2), (3), and (10). In terms of numerical simulations, if a solution of the (discretized) differential MHD equations for an erupting flux rope is obtained [e.g., *Wu et al.*, 1999; *Antiochos et al.*, 1999; *Amari et al.*, 2000; *Linker et al.*, 2001; *Tokman and Bellan*, 2002; *Roussev et al.*, 2003] and if the simulated forces are integrated over the flux rope volume, equation (8) will approximate the resulting macroscopic force. The toroidal forces, originally derived by *Shafranov* [1966] for complete toroidal equilibria and first introduced into the study of the dynamics of solar flux ropes with fixed footpoints by *Chen* [1989], have been invoked for axisymmetric flux-rope geometries [e.g., *Lin et al.*, 1998; *Wu et al.*, 1999; *Titov and Démoulin*, 1999].

3.4. Temporal and Spatial Scales of Driving Forces

[38] We now examine the acceleration process governed by the model equations, where the eruption is driven by poloidal flux injection. Let us focus on F_R, equation (7), at the onset of eruption. Neglecting the gravity and drag terms F_g and F_d, which do not materially affect the discussion in this section, equation (8) can be rewritten as

$$\frac{d^2Z}{dt^2} \approx \frac{V_{Aa}}{\tau_R} f_R = \frac{R}{\tau_R^2} f_R, \tag{11}$$

where $\tau_R \equiv R/V_{Aa}$ and $V_{Aa} = B_{pa}/(4\pi\bar{\rho})$ is the Alfvén speed based on $B_{pa}(t)$ and $\bar{\rho}(t)$. The quantity f_R describes the deviation from $\mathbf{J} \times \mathbf{B}/c - \nabla p = 0$, where $\mathbf{B}$ includes both the self-field of the flux rope and the overlying field B_c. At $t = 0$, the model flux rope is in equilibrium. Note that $d^2Z/dt^2 = 0$ yields $B_c \propto (a/R)B_{pa} < B_{pa}$ (see *Chen* [1996, equation (15)] for the precise condition). Because $F_d = 0$ at $t = 0$ and $F_g \ll F_R$, $F_R(t = 0) \simeq 0$ in typical cases. As the poloidal flux is injected, the toroidal current increases for a short period of time, increasing B_{pa} and pinch force. At this stage, R has not significantly changed. This makes f_R more positive, exerting an upward net force to initiate the eruption.

[39] Equation (11) shows that if any magnetic energy is added to the initial flux rope, the flux rope responds on the time scale of τ_R, which is a measure of the instantaneous Alfvén transit time inside the flux rope. The stronger the magnetic field and the smaller the mass density inside the flux rope, the shorter this time scale is. We refer to τ_R as the "inertial time scale" for the major radial expansion. If the new flux is added over a much shorter time period than τ_R, the subsequent motion is simply response on the time scale of τ_R to an impulsive addition of energy. In the other limit, if the new flux is added over a much longer period of time than τ_R (e.g., quasi-statically), the acceleration initially follows the $\Phi_p^2(t)$ profile.

[40] The linear analyses of equation (11) and d^2a/dt^2 (not discussed here) show that $Z(t)$ is initially exponential with the growth time $\tau_R/f_R^{1/2}$ for both $B_c = 0$ [*Chen*, 1989] and $B_c \neq 0$ [*Cargill et al.*, 1994] cases, where f_R has been linearized in these analyses. This is consistent with the observationally inferred exponential [*Vršnak*, 2001; *Alexander et al.*, 2002; *Gallagher et al.*, 2003; *Shanmugaraju et al.*, 2003] and power-law [*Kahler et al.*, 1988] profiles. The expression, $\tau_R/f_R^{1/2}$, is also the major radial normal mode time scale.

[41] The acceleration can also be expressed in terms of the geometrical size of the flux rope. Dropping the weakly time-dependent $\mathcal{M}_T$ and Θ, the small gravitational force f_g, and the initially-small drag force f_d from equation (9), we find

$$\frac{d^2Z}{dt^2} \sim \frac{\Phi_p^2}{\left[R\ln\left(8R/a_f\right)\right]^2} f_R, \tag{12a}$$

where equation (5) has been used. It is revealing to define

$$k_R \equiv \frac{1}{R\ln\left(8R/a_f\right)}. \tag{12b}$$

Then, equation (12a) takes on the form

$$\frac{d^2Z}{dt^2} \sim k_R^2(t)\Phi_p^2(t) f_R(t). \tag{12c}$$

The factor k_R^2 arises from $F_R \propto I_t^2 \propto L^{-2}$ and represents the inductive properties of an expanding flux rope. Another way to understand equation (12c) is to note that the major radial curvature of the flux rope is $\kappa \equiv 1/R$ so that $k_R \propto \kappa$ and $F_R \propto \kappa^2$.

[42] As the apex height Z increases, the behavior of d^2Z/dt^2 is determined by the evolution of R. Equation (10) shows that R is minimum ($dR/dZ = 0$) at the critical height Z_* defined by

$$Z_* = \frac{S_f}{2}. \tag{13}$$

At $Z = Z_*$, the flux rope is a semicircle. If the flux rope is initially flatter than a semicircle ($Z < Z_*$), R decreases with increasing Z, reaching minimum at $Z = Z_*$. Thus, k_R^2, or equivalently κ^2, is maximum at $Z = Z_*$. Once the flux rope becomes taller ($Z > Z_*$), further increase in height causes k_R to decrease.

[43] This geometrical effect is schematically shown in Figure 6. The three arcs (1, 2, 3) represent a rising flux rope with fixed footpoints. Arc 1, with major radius R_1, is shown with its apex lower than Z_*. Arc 2 is a semicircle with the apex at $Z = Z_*$ with $R_2 = Z_*$. Arc 3 is taller than a semicircle, with the apex at $Z = 2Z_*$. It is easy to see that $R_2 < R_1, R_3$. Recall that we use the term "apex" to denote the centroid, rather than the leading edge, of the model CME (Figure 5).

[44] We denote by $\tilde{Z}_*$ the actual height where the acceleration is maximum. This height is determined by the maximum of the product $k_R^2\Phi_p^2 f_R$ (equation (12c)) and must be obtained by solving the full coupled differential equa-

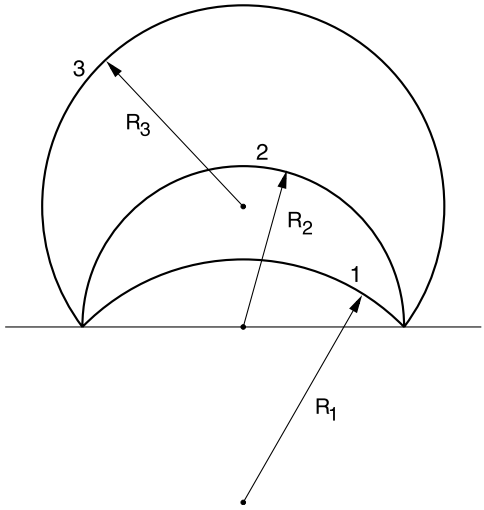

Figure 6. Schematic of a rising flux rope represented by arcs 1, 2, and 3. The radius of curvature (R) first decreases (arc 1 to arc 2) and then increases (arc 2 to arc 3). The radius of curvature is minimum for arc 2: $R_2 < R_1$, R_3. The curvature of the flux rope is $\kappa \equiv 1/R$. Curvature is maximum for arc 2; $\kappa_2 > \kappa_1$, κ_3. The semi-circle geometry yields the critical height $Z_* = S_f/2$, equation (13).

tions for $Z(t)$ and $a(t)$. Because the latter two factors are increasing functions, we have $\tilde{Z}_* > Z_*$. This caveat will be understood throughout this paper. We note that it is $\tilde{Z}_*$ that is more directly relatable to observed acceleration profiles than Z_*.

[45] The rapid decrease in the initial acceleration is due to the geometrical effect embodied in k_R^2. We can infer additional properties of the initial acceleration from k_R^2. For the acceleration immediately after reaching $Z \simeq Z_*$, equation (12a) can be approximated by

$$\frac{d^2Z}{dt^2} \simeq \hat{k}_R^2 \left(\frac{d^2Z}{dt^2}\right)_*, \tag{14a}$$

where $(d^2Z/dt^2)_*$ denotes the peak value of acceleration obtained by substituting equation (13) into equation (12a). The quantities neglected in equation (12a) are now put back in $(d^2Z/dt^2)_*$. Here, $\hat{k}_R$ is k_R normalized to the value at $Z = Z_*$ where $R_* = S_f/2$:

$$\hat{k}_R(R; S_f, a_f) \equiv \frac{(S_f/2)\ln(4S_f/a_f)}{R\ln(8R/a_f)}. \tag{14b}$$

We see from equations (13) and (14b) that the larger S_f is, the higher in the corona the acceleration maximum occurs and the higher into the corona the acceleration persists.

[46] Let Z_m be the apex height where $\hat{k}_R$ has decreased by a specified factor of χ;

$$\hat{k}_R = \frac{1}{\chi}. \tag{15}$$

Then, at $Z = Z_m$, the acceleration is reduced by a factor of χ^{-2} from the peak value $(d^2Z/dt^2)_*$. For a specified value of χ and parameters S_f and a_f, the apex height Z_m corresponding to this point can be obtained by solving

$$\left(\frac{8R}{a_f}\right)\ln\left(\frac{8R}{a_f}\right) = \chi\left(\frac{4S_f}{a_f}\right)\ln\left(\frac{4S_f}{a_f}\right), \tag{16}$$

where $S_f/a_f > 4$. Solving this transcendental equation for R yields R_m satisfying equation (15), which is substituted into equation (10) to obtain Z_m.

[47] For the values of S_f/a_f relevant to our discussion, the solution of equation (16) can approximated by

$$R_m \simeq 0.8\chi Z_*, \tag{17a}$$

which leads to, via equation (10),

$$Z_m \simeq \left[\chi + \left(\chi^2 - 1\right)^{1/2}\right] Z_* \simeq 1.5\chi Z_*. \tag{17b}$$

The numerical factor 0.8 in equation (17a) is a good approximation for $\chi = 2$–3. For more accuracy, it can be replaced by 0.84 for $\chi = 2$ and by 0.77 for $\chi = 3$.

[48] The significance of this height is that the bulk of the acceleration is limited to $Z \lesssim Z_m$, being sharply reduced by the factor $\hat{k}_R^2$. We define the stage of acceleration for $Z < Z_m$ as the "main acceleration phase." The subscript "m" refers to the main phase.

[49] Above Z_m, the driving force continues to decrease, and the flux rope becomes more strongly influenced by the drag term, f_d, equation (9). We define this stage ($Z > Z_m$) of declining Lorentz self-force as the "residual acceleration phase." During this phase, the flux-rope dynamics are determined by the competition between the Lorentz self-force and drag force, and the flux rope may undergo deceleration. This is in contrast to the main phase, during which the Lorentz self-force (all the terms except for the B_c/B_{pa} term in F_R) and the B_c/B_{pa} term are by far the largest competing contributions. We distinguish between the main and residual acceleration phases based on this difference in the action of the various forces. We will provide a more detailed discussion of the main acceleration phase in section 4.2.

[50] As in the definition of Z_*, the derivation of Z_m neglects the increasing functions Φ_p^2 and f_R. In addition, as the acceleration enters the residual phase, the influence of f_d becomes important, and the simple equation (14) becomes invalid. We denote by $\tilde{Z}_m$ the actual height where the acceleration decreases to χ^{-2} of the maximum value. In general, $\tilde{Z}_m > Z_m$. Because the Lorentz force does not necessarily dominate in the residual acceleration phase, $\chi \geq 3$ is not meaningful. As a result, we choose $\chi = 2$ as the definition of the main acceleration phase.

[51] The scaling dependence on S_f embodied in $\hat{k}_R^2$ is universal, dependent only on the physics of the Lorentz hoop force and the toroidal geometry with fixed footpoints. The basic height scales, Z_* and Z_m, are modified by a number of specific effects, yielding $\tilde{Z}_*$ and $\tilde{Z}_m$, which can be directly related to observed CME acceleration profiles. The fundamental scaling ($\propto S_f$), however, is not altered, and we see quite generally that

$$Z_* < \tilde{Z}_* < Z_m < \tilde{Z}_m. \tag{18}$$

[52] The form of equations (13) and (17) results from the geometrical simplification in equation (10) that assumes uniform R. A realistic solar flux rope is likely to have nonuniform R. Nevertheless, if we interpret R as the average radius of curvature near the apex, the gist of the discussion is applicable.

[53] We point out that for flux ropes with small S_f and short τ_R, the critical height $\tilde{Z}_*$ may be reached so soon after eruption that the main phase may not be resolvable. This scenario may be relevant to eruption of small filaments.

[54] We close this subsection by pointing out an important role of the inductance. The geometrical effect (Figure 6) and the scaling properties embodied in equations (13) and (14) arise from the inductive property, equation (5), of a 3-D flux rope with fixed footpoint separation S_f. The inductance of a flux rope, which is intrinsic to Maxwell's equations, simply relates the magnetic energy of the flux rope to the current and varies as the flux rope evolves. Thus the inductance couples the expansion motion of the flux rope to the flux-rope current and hence the Lorentz force. This is a fundamental difference between the inductance of a plasma structure and that of an "electric circuit" model consisting of fixed elements.

4. Application to Observed CME Events

[55] Equations (12), (13), (14), and (17b) identify the footpoint separation distance S_f as the natural scale length that governs the initial acceleration process. To quantitatively test the scaling law, we need sufficiently detailed observations throughout the FOV of C1, C2, and C3. Although equations (13) and (14) suggest that the most prominent signatures of acceleration should be in the C1 and perhaps C2 FOV, C3 data provide an additional constraint on the model solutions. For our discussion, we will use the three CMEs shown in Figures 1–3 as a testbed for the theory.

[56] The procedure to model specific CMEs has been detailed elsewhere [*Wood et al.*, 1999]. Briefly, the first step is to specify the initial flux rope: the footpoint separation, S_f, and the apex (centroid) height, Z_0. The initial major radius R_0 is then given by equation (10), and we specify a_0. We have found that $R_0/a_0 = 2–2.5$ usually yields the best agreement. The ambient coronal parameters, $p_a(Z_0)$, density $n_a(Z_0)$, and overlying field $B_c(Z_0)$ are determined from the previously specified background model. We typically choose the initial flux-rope plasma density $\overline{n}(Z_0)$ to be $n_a(Z_0)/2$ and the temperature to be the same (2×10^6 K) in and outside the flux rope. The initial magnetic field and mass of the flux rope are then calculated by demanding force balance in the major and minor radial directions. This yields $\overline{B}_t$, B_{pa}, and the total mass, $\mathcal{M}_T$, as output of the model. For our model calculations here, the initial mass is assumed to be equally divided between the hot cavity plasma and cold prominence material for lack of specific estimates based on observations. If $\overline{n}(Z_0) = n_a(Z_0)/2$, the initial equilibrium is neutrally buoyant, i.e., $f_g(t = 0) = 0$, so that $f_R(t = 0) = 0$. The prominence mass is drained out (but with 15% of the initial mass entrained in the flux rope) on the time scale of 2 hours.

[57] Occasionally, observational indicators such as magnetic neutral lines and the height of emission features associated with the eruptive structure are available. In such cases, we use them as proxies for S_f and Z_0, respectively [e.g., *Chen et al.*, 2000].

[58] Having specified the initial flux rope, the only parameter used to match the observation is the flux "injection" function $d\Phi_p(t)/dt$. This gives $\Phi_p(t) = \int (d\Phi_p/dt)\, dt + \Phi_{p0}$, which enters the calculation via equation (9). Here Φ_{p0} is the poloidal flux of the initial flux rope. The requirement that the calculated leading-edge height-time and speed-time curves match the observed data then yields, as output of the theory, the poloidal flux injection rate function $d\Phi_p(t)/dt$ that provides the best fit to the observed data for the specified initial flux rope. However, if the footpoint separation S_f is not suitable, it is generally not possible to find a good fit. If so, S_f is varied, and the procedure is repeated until a good fit is obtained. In such cases, S_f is also an output of the model.

[59] The function $d\Phi_p(t)/dt$ represents a packet of poloidal flux: it is increased from zero or a small value to the peak value using hyperbolic tangent with a time constant of λ_1; the peak value is held constant for a duration of $\delta > 0$; it asymptotically decreases to zero according to a hyperbolic tangent function with a time constant of λ_2. We allow λ_1 and λ_2 to be unequal. This functional form is the same as that used in our previous studies.

[60] It is important to note that increasing Φ_p is not equivalent to increasing the toroidal current I_t: if the flux rope expansion, i.e., the increase in the inductance, becomes sufficiently fast, I_t can decrease even as Φ_p is increased. This situation corresponds to the condition

$$\frac{1}{\Phi_p}\frac{d\Phi_p}{dt} < \frac{1}{L}\frac{dL}{dt}, \tag{19}$$

which follows from $I_t(t) = \Phi_p(t)/cL(t)$ (equation (2)). This occurs when the centroid height Z exceeds the critical height $\tilde{Z}_*$. Until then, I_t increases with increasing Φ_p (section 6).

4.1. Specific CME Events: Main Acceleration Phase

[61] We illustrate the results discussed in section 3 using the "best fit" solutions for the CMEs shown in Figures 1–3. In obtaining these fits, we attempt to reproduce the peak speed and the residual acceleration phase in the C2-C3 FOV. This provides a strong constraint on the overall fit and determines the range of values of λ_1, λ_2, and δ for optimum agreement.

4.1.1. 23 February 1997 CME

[62] We set the initial height of the apex centroid at $Z_0 = 10^5$ km from the solar surface and footpoint separation at $S_f = 3.7 \times 10^5$ km, yielding major radius $R_0 = 2.2 \times 10^5$ km. We choose $R_0/a_0 = 2.5$. From the equilibrium force balance condition, we obtain the initial flux-rope magnetic field of $B_{pa} = 2.9$ G and $\overline{B}_t = 3.4$ G, corresponding to $I_t = 1.3 \times 10^{11}$ A, and the total mass of $\mathcal{M}_T \simeq 8.6 \times 10^{15}$ g. Here, we have used $\overline{n} = n_a(Z_0)/2 \simeq 2.4 \times 10^8$ cm^{-3} and $B_c(Z_0) = -1$ G. For these parameter values, $\beta_p(t = 0) = 8\pi(\overline{p} - p_c)/B_{pa}^2 = -0.37$, meaning that the cavity pressure is lower than the background coronal pressure. The plasma β is $\sim$0.16. The SW speed is ramped up to $V_{sw} = 400$ km s^{-1} at $\sim 20\, R_\odot$.

[63] The solid curves in the top three panels of Figure 1 show the theoretical height, speed, and acceleration, respectively, of the leading edge. The dotted curves are the height, speed, and acceleration of the centroid of the apex. Recall

that the leading edge and centroid positions are related by $Z(t) + 2a(t)$ and that the other quantities are the appropriate time derivatives. The profile of $d\Phi_p(t)/dt$ for this solution is given in units of 2×10^{18} Mx s^{-1} by the dashed curve in Figure 1b. The peak flux injection rate is $\sim 9 \times 10^{18}$ Mx s^{-1}. The poloidal flux $\Phi_p(t)$ is a monotonically increasing function, with the initial value $\Phi_{p0} = 1.8 \times 10^{21}$ Mx. A total of 3×10^{22} Mx in poloidal flux is injected in approximately 70 min. The ramp-up time constant is $\lambda_1 = 14.5$ min, the ramp-down time constant is $\lambda_2 = 20$ min, and the peak injection rate is held constant for $\delta = 20$ min. The $d\Phi_p/dt$ function is ramped up in 75 min using λ_1 starting at time $T = 0127$ UT in this figure. The present solution, while similar to that of *Wood et al.* [1999], is not identical because the initial geometry is not identical, but it is well within the range of good fits presented by Wood et al. for both leading-edge and centroid data.

[64] It is evident that the solution correctly fits the observed leading edge motion throughout the C1-C2-C3 FOV. In particular, the acceleration peak is well described by equations (12)–(14). This can be seen as follows. In Figure 1d, we have plotted k_R^2 (solid curve), f_R (dashed curve), and mass $\mathcal{M}_T$ (dash-dot curve). The k_R^2 and $\mathcal{M}_T$ curves are normalized to the initial values. We do not show $\Phi_p(t)$, but it can be inferred from $d\Phi_p/dt$ in Figure 1b. The centroid acceleration is given by the product of $k_R^2\ \Phi_p^2 f_R$ (equation (12c)). As pointed out earlier, because the latter two are increasing functions of time, the maximum acceleration occurs after the peak in k_R^2. In this figure, k_R^2 reaches the maximum value at time $T = 0216$ UT, corresponding to the critical height $Z_* = 1.85 \times 10^5$ km from the surface (equation (13)). The centroid acceleration given by the full solution is shown by the dotted curve in Figure 1c: the peak acceleration is ~ 550 m s^{-2} and occurs at $\tilde{Z}_* \simeq 4.9 \times 10^5$ km at time $T = 0246$ UT. The minor radius at this time is $a = 9.5 \times 10^4$ km, yielding the leading edge height of $Z + 2a = 6.8 \times 10^5$ km.

[65] For this model flux rope, k_R^2 decreases to 1/4 of its maximum value at apex height of $Z_m \simeq 1.5\chi Z_* = 5.5 \times 10^5$ km, where $\chi = 2$ according to our definition. This corresponds to $T \simeq 0250$ UT. The centroid acceleration of the full solution decreases to 1/4 of its maximum value at $\tilde{Z}_m \simeq 1.1 \times 10^6$ km and $T \simeq 0300$ UT. For this event we indeed have $Z_* < \tilde{Z}_* < Z_m < \tilde{Z}_m$ in accord with equation (18). Evidently, the interplay between the different factors in the product $k_R^2 \Phi_p^2 f_R$ discussed above is correctly reflected in the observed acceleration.

[66] The leading-edge acceleration is given by $d^2(Z + 2a)/dt^2$, the minor radial acceleration being equal to the difference between the solid curve and dotted curve in Figure 1c. For $Z \lesssim Z_*$, increasing Φ_p causes I_t to increase, which tends to increase pinch force. For $Z > Z_*$, k_R and therefore the toroidal current $I_t \propto k_R$ decrease. This decreases pinch force, allowing the minor radius to expand more freely. As a result, $d^2 2a(t)/dt^2$ has its maximum value after k_R begins to decrease, approximately coinciding with the period of fastest decrease in k_R. For this model flux rope, the leading edge has maximum acceleration (676 m s^{-2}) at $T \simeq 0244$ UT and $Z \simeq 4.6 \times 10^5$ km, with $d^2 2a(t)/dt^2 \simeq 129$ m s^{-2}.

[67] Figure 1d shows that the flux rope mass $\mathcal{M}_T$ is nearly constant, justifying a posteriori the assumption of weakly time-dependent $\mathcal{M}_T$ in obtaining equation (12a).

[68] The inertial time scale τ_R (equation (11)) is $\tau_R \simeq 13$ min in this case. This is comparable to the time constant of flux injection, λ_1, but is shorter than the ramp-up duration of 75 min. It is clear from Figures 1c and 1d that the overall decline in the main acceleration arises entirely from the rapid decrease in k_R^2 for $Z > Z_*$. The slight dip in the centroid acceleration arises from the dip in f_R.

[69] Subsequent to the main phase, i.e., $Z > Z_m$, the CME exhibits slow and declining acceleration and possibly deceleration of comparable magnitude. At this stage, the factor k_R^2 has reduced the magnitude of F_R to the point where the drag term F_d becomes comparable, possibly resulting in deceleration. The drag force, $F_d \propto (V_{sw} - V)|V_{sw} - V|$, typically peaks after the main phase. This is balanced by the fact that as the flux rope expands away, the ambient SW speed also increases, tending to reduce the speed differential. The CME motion after the main phase is primarily determined by the competition between the residual Lorentz self-force, which depends on how long the flux injection is sustained (section 4.3), and the drag force. The precise contributions from various terms in equation (7) are different in the two regimes ($Z < Z_m$ versus $Z > Z_m$) and will be examined more closely in section 4.3.

[70] Note that the acceleration reaches the peak value and begins to decrease even before $d\Phi_p(t)/dt$ attains the maximum (Figures 1b and 1c). Thus only a fraction of the total flux to be injected has been injected before the main acceleration is finished. Therefore the peak acceleration and the main phase ($Z < Z_m$) are largely insensitive to the duration of the flux injection or to how much total flux is injected.

[71] The CME of 9 September 1997 is similar in the basic dynamical properties to this event, as are the details of the physics [*Chen et al.*, 2000]. Several CMEs modeled by *Krall et al.* [2001] are also similar.

4.1.2. 30 April 1997 CME

[72] For this event, we use $Z_0 = 10^5$ km and footpoint separation $S_f = 3.3 \times 10^5$ km. The major radius is $R_0 = 1.9 \times 10^5$ km, and the aspect ratio is $R_0/a_0 = 2.5$. This flux rope is similar to that used by *Wood et al.* [1999] to model this event. The flux rope density is $\overline{n} = n_a(Z_0)/2 = 2.4 \times 10^8$ cm^{-3}. The equilibrium conditions yield as initial values $\mathcal{M}_T \simeq 5.6 \times 10^{15}$ g, $\overline{B}_t = 3.4$ G, and $B_{pa} = 2.9$ G, corresponding to $I_t = 1.1 \times 10^{11}$ A. The plasma β in the flux rope is 0.16, and $\beta_p = -0.38$. As before, we assume $V_{sw} = 400$ km s^{-1}. The flux injection function required for the best fit is shown in units of 6×10^{17} Mx s^{-1} l (dashed curve, Figure 2b), with the peak flux injection rate $\sim 8 \times 10^{17}$ Mx s^{-1}. The initial poloidal flux is $\Phi_{p0} = 1.4 \times 10^{21}$ Mx, and a total of $\sim 1.4 \times 10^{22}$ Mx in poloidal flux is injected in approximately 6 hours. The form of $d\Phi_p/dt$ is specified by $\lambda_1 = 30$ min, $\lambda_2 = 110$ min, $\delta = 145$ min. The flux injection function is ramped up in 65 min.

[73] The solid and dotted curves in Figure 2 show the calculated dynamics of the leading edge and centroid of this flux rope. Overall, the height, speed, and acceleration profiles are well reproduced by the solution, but if the acceleration value of ~ 140 m s^{-2} at the second peak is true, the solution does not fit this point well. However, the solution is consistent with the lower end of the error bar for this point. Aside from the precise values, the slight "hesitation" shown in the speed data appears real. In fitting

the observed speed data, we did not attempt to fit the details (specifically, the dip) of the initial acceleration. It is interesting that all the solutions we have obtained that yield reasonable fits to the nearly constant speed data points in C2 and C3 FOV have this dip.

[74] Although this CME exhibits more pronounced oscillatory behavior early in the eruption than the 23 February event, it is clear that the main acceleration has already ceased when the leading edge enters the C2 FOV. For this solution, the maximum k_R^2 occurs when the centroid of the apex reaches $Z_* \simeq 1.65 \times 10^5$ km and $T \simeq 0346$ UT, which is before $d\Phi_p/dt$ reaches its maximum value. At this point, $a = 7.9 \times 10^4$ km, and the leading edge is at $(Z + 2a) = 3.2 \times 10^5$ km above the photosphere, corresponding to the first of the two peaks. Subsequently, k_R^2 decreases, but the rapidly increasing f_R, multiplied by Φ_p^2, causes the second and the main peak (70 m s^{-2}) in the centroid acceleration. This occurs when the apex is at $\tilde{Z}_* = 4.4 \times 10^5$ km s^{-1}, which roughly corresponds to the height of fastest decrease in k_R^2 and, as in the case for the 23 February event, to the maximum minor radial acceleration. The minor radius is $a \simeq 1 \times 10^5$ km, and the leading edge is at $Z + 2a = 6.4 \times 10^5$ km. The leading edge acceleration at this point is $\sim$93 m s^{-2}.

[75] The factor k_R^2 decreases from its maximum by a factor of $\chi^{-2} = 1/4$ when the apex reaches $Z_m \simeq 1.5 S_f \simeq 5 \times 10^5$ km at $T = 0421$ UT. The actual centroid acceleration decreases to 1/4 at $\tilde{Z}_m = 7.2 \times 10^5$ km s^{-1} at $T \simeq 0450$ UT. At this point, $a \simeq 1.4 \times 10^5$ km so that leading-edge height is $(Z + 2a) \simeq 1 \times 10^6$ km above the solar surface, which is slightly above the inner edge of the C2 FOV (vertical dashed line). This height marks the transition from the main to residual acceleration phase. In agreement with equation (18), we have $Z_* < \tilde{Z}_* < Z_m < \tilde{Z}_m$, which includes the effects of f_R and Φ_p^2.

[76] The main acceleration phase, corresponding to the single peak in k_R^2, encompasses the two pronounced peaks in the centroid as well as leading edge acceleration. The dip is caused by the interplay of various force contributions to the factor f_R (section 4.2).

4.1.3. 2 June 1998 CME

[77] The above solutions indicate that a footpoint separation distance of $S_f \sim R_\odot/2$ is consistent with the spatial scales evident in the acceleration profiles of both CMEs, each having the acceleration maximum below $\sim$1 $R_\odot$ from the surface. However, the magnetic field footpoints cannot be clearly identified for these CMEs. We now further test the results, equations (13), (14), and (17) against a CME with the main acceleration phase occurring at a much greater height.

[78] The 2 June 1998 CME was associated with a large polar crown prominence near the south pole. This well-known LASCO event has been reported by *Plunkett et al.* [1999]. Successive Hα images of the prominence over several days preceding the CME suggest that the prominence was about 3/4 $R_\odot$ in length. Figure 7a shows the polar crown prominence near the southwest limb on 28 May 1998 at 0000 UT, courtesy of the Big Bear Solar Observatory (BBSO). If the prominence is suspended inside a flux rope [*Low and Hundhausen*, 1995; *Chen*, 1996], the actual flux rope footpoint separation should be comparable to or possibly greater than the prominence length. The prominence rotated behind the southwest limb about 1 day before the eruption.

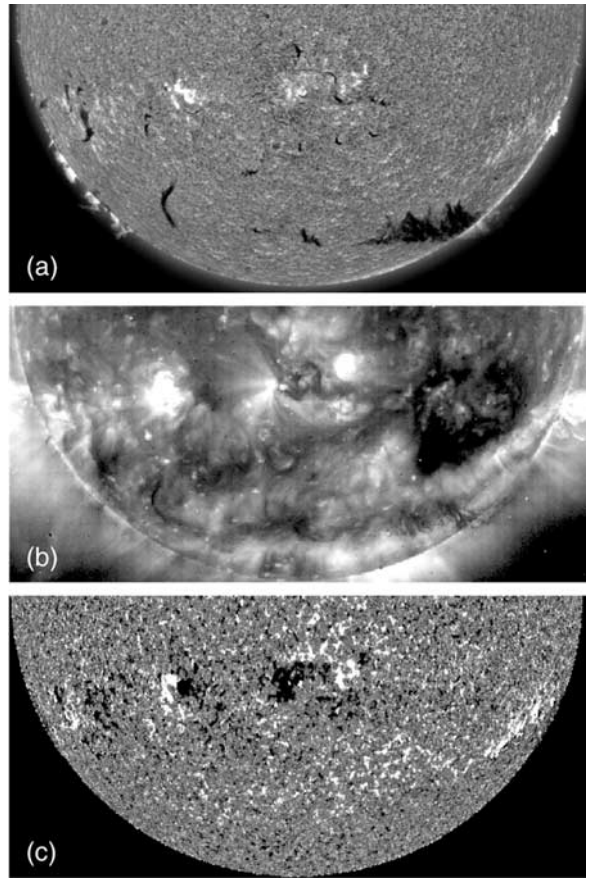

Figure 7. (a) Big Bear Solar Observatory H_α image of the southern polar crown at 0000 UT, 28 May 1998. (b) EIT (195 Å) image of the same region at 906 UT, 28 May 1998. (c) Magnetogram at 1400 UT, 28 May 1998, obtained by the National Solar Observatory at Kitt Peak. (Courtesy H. Wang).

[79] In modeling the observed motion and expansion of this CME shown in Figure 3, we first used the same initial flux rope as the one used to model the 23 February 1997 CME with $S_f \simeq 0.53$ $R_\odot$. We then varied the flux injection profile $d\Phi_p/dt$ to see if it is possible to fit the LASCO data. We found that it is possible to obtain solutions with nearly constant speeds at about 1000 km s^{-1} but that with the acceleration profiles invariably peaked below $\sim$2 $R_\odot$ (heliocentric) even if the ramp-up time constant is made long. Such solutions are similar to the one shown in Figure 1 but are in poor agreement with the data for the 2 June 1998 CME.

[80] We now set $S_f = 1.8 R_\odot = 1.26 \times 10^6$ km. We choose $Z_0 = 3.25 \times 10^5$ km so that $R_0 = 7.7 \times 10^5$ km. Because of the height, we choose $B_c = -0.25$ G and $\overline{n} \simeq 5 \times 10^7$ cm^{-3}. We set $R_0/a_0 = 2.5$, giving $a_0 = 3.1 \times 10^5$ km. The equilibrium force balance yields $B_{pa} \simeq 1$ G and $B_t \simeq 1.3$ G, corresponding to $I_t = 1.5 \times 10^{11}$ A. We also obntain $\mathcal{M}_T = 7.3 \times 10^{16}$ g. For this flux rope, $\tau_R \simeq 30$ min. Figures 3a–3c show the calculated leading edge (solid curves) and centroid (dotted curves) height, speed, and acceleration, respectively. We see that this model flux rope with $S_f = 1.8$ $R_\odot$ yields good quantitative agreement with the observed CME dynamics

throughout the LASCO FOV. Most notably, the leading-edge acceleration is peaked at $\sim$3.5 $R_\odot$ from Sun center, and the speed continues to increase in the C3 FOV.

[81] The poloidal flux injection rate $d\Phi_p/dt$ for this solution is given in Figure 3b in units of 5×10^{17} Mx s^{-1} (dashed curve). The maximum injection rate is 2.5×10^{18} Mx s^{-1}, and a total of 4.9×10^{22} Mx in poloidal flux is injected. The flux injection rate increases with a time constant of λ_1 = 30 min over 100 min and decreases with a time constant of λ_2 = 130 min. The maximum rate is held constant for δ = 160 min. The long ramp-down time constant λ_2 in comparison with λ_1 is necessary to fit the small residual acceleration seen near the outer edge of C3. Because of the high latitude, we increased the SW speed to V_{sw} = 600 km s^{-1} at $\sim$20 $R_\odot$. Compared with using V_{sw} = 400 km s^{-1} (with the same functional form), the leading-edge speed of this solution is faster by $\sim$50 m s^{-2} at 20 $R_\odot$, with virtually no discernable difference at 10 $R_\odot$. Most of the flux is injected over 4–5 hours, which is considerably longer than the duration of the main acceleration phase. As before, we have adjusted the maximum injection rate and the time constants, λ_1, λ_2, and δ. We have varied the duration δ of the peak injection rate from 80 min to 240 min and found the results to be insensitive: at 30 $R_\odot$, the leading-edge speeds are within $\sim$50 km s^{-1} of the solution shown in Figure 3.

[82] Figure 3d shows the functions k_R^2 (solid) and f_R (dashed) defined in section 3. Comparing k_R^2 and the centroid acceleration (dotted curve) in Figure 3c, we can clearly identify the main acceleration phase. The maximum of k_R^2 occurs at $Z_* = 6.3 \times 10^5$ km and decreases by a factor of $\chi^2 = 4$ at $Z_m \simeq 1.5\chi Z_* = 2.7\ R_\odot = 1.9 \times 10^6$ km. The actual centroid acceleration (dotted curve) attains maximum value of $\sim$104 m s^{-2} at height $\tilde{Z}_* \simeq 8 \times 10^5$ km and time $T \simeq$ 0954 UT in this figure. The main acceleration phase ends at $\tilde{Z}_m \simeq 4.6 \times 10^6$ km and T = 1206 UT. This solution yields a relatively extended main acceleration phase because of the continued flux injection, which sustains the significant residual acceleration with a nearly constant value during 1200–1400 UT. The condition $Z_* < \tilde{Z}_* < Z_m < \tilde{Z}_m$ is readily satisfied.

[83] For completeness, we note that the calculated leading edge attains maximum acceleration, 155 m s^{-2}, at $Z \simeq$ 2.6 $R_\odot$ above the solar surface at $T \simeq$ 1013 UT. As in the preceding two examples, the minor radial acceleration attains maximum value where the decrease in k_R^2 is steep.

[84] We have also sought solutions for S_f = 1.5 $R_\odot$ and S_f = 2 $R_\odot$. The dash-dot curves in Figures 3a–3c show the leading edge height, speed, and acceleration, respectively, of the best-fit solution with S_f = 1.5 $R_\odot$. We see that in all three quantities, the solid and dash-dot curves are nearly identical and are well within error bars. Evidently, the solutions are insensitive to the precise choice of S_f values provided S_f is greater than $\sim$1.5 $R_\odot$. Thus we conclude, as output of the calculation, that the underlying magnetic flux rope must have a footpoint separation distance in the range of 1.5–2 $R_\odot$. This is considerably longer than the H_α filament.

[85] To test this conclusion, we have examined the EIT images and magnetograms obtained before the eruption and found that indeed the H_α filament was located inside a much longer filament channel. Detailed examination of H_α images obtained over a few days prior to the eruption (Figure 7a shows one such image) reveals features that suggest a filament channel extending westward (around the west limb in this image) and eastward. In particular, the curved filament near the southeast limb appears to be part of the filament channel. Figure 7b shows the EIT (195 Å) image of the south pole on 28 May 1998. We see a long, dark filament channel that spans the polar crown region from east to west (with the western most part already behind the limb). In this EIT image, it is possible to identify absorption features that correspond to the large H_α prominence and the curved filament at the eastern end of the filament channel. Comparing the two images, we see that the H_α prominence is slightly south of the EIT filament channel, indicating the prominence is higher in the corona. In Figure 7c, we show an enhanced magnetogram (data courtesy of National Solar Observatory at Kitt Peak and the image courtesy of H. Wang of New Jersey Institute of Technology). We see a magnetic neutral line corresponding to the EIT filament channel. Taken together, we conclude that the large polar crown filament was associated with a much longer magnetic field structure.

[86] The large H_α prominence rotated behind the limb on 1 June 1998. However, after the eruption on 2 June 1998, a posteruption arcade along the filament channel was observed in EIT images. We regard this as supporting evidence of the interpretation that the filament channel corresponded to or contained a magnetic flux rope extending from the backside to the frontside around the southwest limb. In our calculation, we have placed the apex of the flux rope in the plane of the sky. If this interpretation is correct, the result $S_f \simeq$ 1.5–2 $R_\odot$ demanded by the model for a good fit is indeed consistent with the initial magnetic structure underlying the eruptive prominence. We emphasize that the need to set S_f = 1.5–2 $R_\odot$ was compelled by the requirement to match the main acceleration phase, with the peak acceleration at $\sim$3.5 $R_\odot$, and by the inability to find a solution to fit the data with $S_f < 1\ R_\odot$. We add that for the 9 September 1997 CME whose main acceleration phase was observed MK3, the observed neutral line length of the candidate source region was used as a proxy for S_f, yielding good agreement with the MK3-LASCO data [*Chen et al.*, 2000].

4.1.4. Eruptive Prominences

[87] Although magnetic footpoints are not directly observed, some eruptive prominences appear to have nearly stationary footpoints relative to the apex. For example, *Vršnak* [1990a] and *Vršnak et al.* [1993] have described the dynamics of two such eruptive prominences. Using the observed H_α prominence as a proxy for the trailing edge of a flux rope and assuming R/a = 2.5, we can obtain from the observed prominences the heights at which the centroids of the inferred flux ropes attain their maximum values. We find that the results are consistent with equation (18). Here, we assume that the projection effect is small for both events.

4.2. Complex Features of CME Acceleration

[88] Although the acceleration profiles of the CMEs in Figures 1–3 appear different, they are dynamically quite similar. All three profiles have the bulk of the acceleration confined to below Z_m (equation (17b)). This means that when scaled to $Z_* = S_f/2$ (equation (14)), the solutions are similar in form, with the main acceleration limited to below

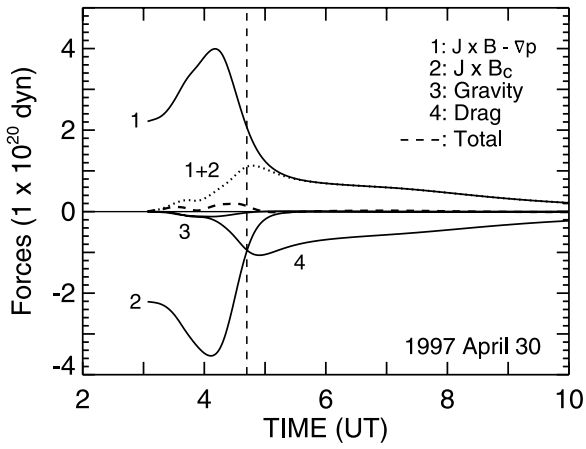

Figure 8. Detailed contributions from the terms in equation (7). The two dominant components are the Lorentz self-force (curve 1) and the external Lorentz force $I_t B_c$ arising from the overlying coronal field B_c (curve 2). The main acceleration, $Z < Z_m$, equation (17b), is determined by these two contributions. The residual acceleration phase ($Z > Z_m$) is largely determined by the competition between the Lorentz self-force and the drag force (curve 4).

approximately $Z_m < 1.5\chi Z_*$. The temporal relationship between the main acceleration and the flux injection function $d\Phi_p/dt$ is also alike for the events: the centroid acceleration reaches maximum and begins to decrease early in the injection process, usually before $d\Phi_p/dt$ reaches its peak value. The main acceleration phase, however, need not consist of one peak, sometimes exhibiting "complexity" characterized by one or sometimes two periods of significantly reduced acceleration or deceleration. Such properties arise from the interplay of various force contributions given in equations (7) and (8). We now examine the specific force terms to illustrate how such complexities can be explained.

[89] We choose the 30 April 1997 CME because it has the most pronounced oscillatory behavior of the three events discussed here. Figure 8 shows a detailed breakdown of the major radial force contributions for the best-fit solution shown in Figure 2. Curve 1 is equal to F_R minus the overlying field term, B_c/B_{pa}, in equation (7). The B_c/B_{pa} contribution is separately shown by curve 2. Thus the dotted curve marked "1 + 2" gives F_R. Curves 3 and 4 are the F_g and F_d terms in equation (8). The dashed curve is the sum of curves 1–4, giving the total force acting on the flux rope. At $t = 0$, all contributions add to zero because of the initial equilibrium force balance.

[90] The peak of curve 1 occurs at $\tilde{Z}_*$ and is determined by $k_R^2 \Phi_p^2 f_R$. The external Lorentz force (curve 2) is $I_t B_c(z)$ and is determined by $I_t \propto k_R$ multiplied by $B_c(z)$ (for which we use the form previously specified [*Chen*, 1996]). We have found that it is the Lorentz self-force (curve 1) and the $I_t B_c$ force (curve 2) that compete during the main acceleration phase. The first dip in the acceleration at $T \simeq 0400$ UT results from this competition. The drag contribution typically becomes important in the residual acceleration phase (section 4.3). The second dip in the acceleration is attributable to the drag term. The overall width of the main acceleration phase is determined by $k_R^2 \Phi_p^2 f_R$, which in this example encompasses the two peaks. We mention that generally, the ∇p contribution, which is included in curve 1, is much smaller than the Lorentz self-force in model flux ropes appropriate for CMEs, indicating that they are nearly force-free. However, it may be comparable to the net force (dashed curve in Figure 8). We have analyzed the force contributions for the 23 February and 2 June CMEs with similar results (not shown here). This has also been shown for a generic CME-like flux rope [*Chen*, 1996, Figure 7] and the 9 September 1997 CME [*Chen et al.*, 2000, Figure 7].

4.3. Residual Acceleration Phase

[91] We have so far focused on the main acceleration phase ($Z < Z_m$). In the residual acceleration phase, all contributions to the driving force decrease because $k_R^2 \ll 1$ for $Z > Z_m$, so that the forces are much smaller than in the main acceleration phase, explaining the near-constancy of CME speeds beyond 3–4 $R_\odot$. Figure 8 shows that the Lorentz self-force (curve 1) and the drag term (curve 4) become the dominant contributions and determine the net force. It is interesting to see what physical effects determine relatively slow ("gradual") acceleration at the C2-C3 FOV heights [*MacQueen and Fisher*, 1983; *Sheeley et al.*, 1999].

[92] In Figure 9, we show two solutions obtained for the initial flux rope used for the 30 April 1997 CME. They correspond to two different $d\Phi_p/dt$ profiles, but all other parameters are identical to those of the solution shown in Figure 2. The solid curve 1 in Figure 9a is the solution for the leading edge. The profile of $d\Phi_p/dt$ (curve 1, Figure 9b)

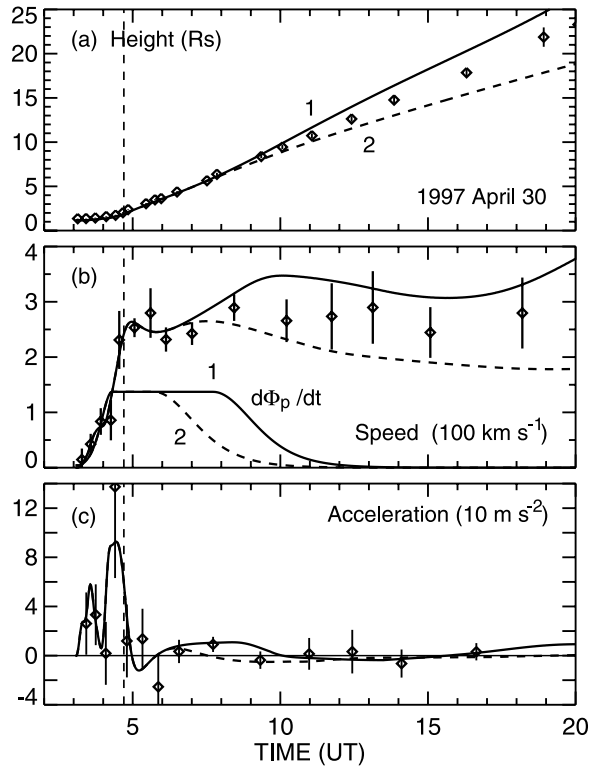

Figure 9. Two solutions with different flux-injection durations for the 30 April 1997 event. Solid curve 1: the peak injection rate is maintained for $\delta = 205$ min. Dashed curve 2: $\delta = 85$ min. The initial flux rope and other parameters are identical to those for the solution shown in Figure 2.

for this solution is the same as that in Figure 2b except that the peak value is maintained 60 min longer, increased from $\delta = 145$ min (Figure 2b) to $\delta = 205$ min (curve 1, Figure 9b). The corresponding leading-edge speed is shown in Figure 9b (thick solid curve). The main acceleration (solid curve, Figure 9c) is unchanged, but there is now greater residual acceleration persisting into the C2-C3 FOV, with the leading-edge speed increasing from $\sim$250 km s^{-1} to 350 km s^{-1} in several hours. This acceleration is considerably less in magnitude than the main acceleration even though the flux injection rate remains at the peak value longer. The increased duration of flux injection only causes the Lorentz self-force (curve 1 in Figure 8) to decrease more slowly with expansion, producing a longer period of residual acceleration.

[93] Conversely, we can shorten the flux injection duration. Dashed curve 2 in Figure 9a is the solution given by a $d\Phi_p/dt$ profile (dashed curve 2, Figure 9b) that is identical to that shown in Figure 2b except that the duration of the peak injection rate is reduced by 60 min to $\delta = 85$ min. The corresponding leading-edge speed is shown in Figure 9b (thick dashed curve). We see that the CME slows down after the main acceleration phase because the residual Lorentz force is not sustained, and the drag term dominates. Similar exercises were carried out for the 23 February 1997 and 2 June 1998 CMEs with qualitatively similar results (not shown). It is generally the case that the long-time dynamics are determined by the interplay of the toroidal Lorentz force and the drag force: because $F_d \propto (V_{sw} - V)|V_{sw} - V|$, if the CME is slower (faster) than the ambient solar wind, it is accelerated (decelerated) by the solar wind [*Chen*, 1996]. This prediction has been borne out by observations [*Gopalswamy et al.*, 2000].

[94] Continued flux injection provides sustained residual acceleration or nearly constant speed at C2-C3 heights for fast CMEs. However, the flux-rope response, which occurs on the inertial time τ_R (equation (11)), becomes slower as the flux rope increases in size ($\tau_R \propto R$). As a result, after the main acceleration phase ($Z > Z_m$), there tends to be no rapid acceleration or deceleration. As a test, we have taken the initial flux rope used to model the 30 April CME and applied a double-peaked injection profile (not shown): the two packets of poloidal flux are each identical to that shown in Figure 2b, but the onset of the second one is delayed by 8 hours, at which point the flux-rope apex has already reached approximately 7 $R_\odot$ (about T = 1100 UT in Figure 2). We find that the second packet increases the acceleration after $T = 1100$ UT by only a small amount from that shown in Figure 2, the overall appearance of the acceleration profile being similar to that shown in Figure 9b (thick solid curve).

[95] Note that the physics of the residual acceleration phase is common to fast and slow CMEs. During this phase, CMEs exhibit small positive or negative acceleration depending on how drag competes with the Lorentz self-force. However, the magnitude of acceleration is small because $k_R^2 \ll 1$, and the characteristic time scale τ_R becomes longer.

5. Model Distribution of Speed-Height Profiles

[96] Equations (13) and (17) imply that the main acceleration of a flux rope with a smaller S_f occurs lower in the corona than that of one with a larger S_f. If active region-associated CMEs are, as a group, more compact than solitary prominence-associated CMEs, these equations can explain the findings of *MacQueen and Fisher* [1983] and *St. Cyr et al.* [1999] that active-region CMEs tend to show little or no residual acceleration. The results of section 4 also show that the ultimate speed at C2 and C3 heights is principally determined by the total amount of poloidal flux or magnetic energy injected while the presence or absence and the magnitude of gradual acceleration at these heights depend on the speed of the CME relative to the SW and on the duration of poloidal flux injection. Additionally, the overlying field B_c influences the amount of energy stored in the initial equilibrium flux rope and thus the main acceleration.

[97] These results suggest that we examine what speed-height distributions may result if a two-parameter spectrum (injected poloidal energy and injection duration) of $d\Phi_p/dt$ profiles is applied to a given initial flux rope and if B_c is varied. Consider a flux rope defined by the apex height, $Z_0 = 1 \times 10^5$ km, footpoint separation distance $S_f = 3 \times 10^5$ km, and $R_0/a_0 = 2.27$. The ambient coronal field at the apex is taken to be $B_c(Z_0) = -1$ G. The initial equilibrium requires a mass of $\mathcal{M}_T = 5.6 \times 10^{15}$ g, $\overline{B}_t = 2.5$ G, and $B_{pa} = 2.6$ G. Based on the magnetic field model described elsewhere [*Chen*, 1996; *Krall et al.*, 2000], the maximum toroidal field is $B_t(r = 0) \simeq 7.5$ G on the axis of the flux rope.

[98] We consider a spectrum of total injected poloidal energies (0.2, 0.5, 0.8, 1.1, 1.4, and 1.7×10^{32} erg) and for each value of energy, a spectrum of injection time scales (1, 3, 5, 7, and 9 hours) defined to be the duration of the full-width at half-maximum of the flux injection profile (e.g., the dashed curves in Figures 1b, 2b, and 3b). Note that the flux injection rate corresponding to the injected poloidal magnetic energy depends on the evolving flux rope dimensions. Thus we adjust the amplitude of the flux injection profile so that the solution yields the energy values specifed above. Therefore the flux injection rate is an output of the calculation. These choices of parameters form a matrix of 30 flux injection conditions evenly spaced in poloidal magnetic energy and injection time duration.

[99] Figure 10a shows the entire set of 30 solutions in the form of centroid speed versus height curves. We use the centroid, rather than the leading-edge, height and speed because the centroid provides the average motion. The figure shows a significant number of model speed-height curves that have large and sustained acceleration at heights of 5–10 $R_\odot$. The sample of C2-C3 CMEs in Figure 4 and the previously published results based on LASCO data [*Sheeley*, 1999] do not appear to show the presence of this population.

[100] In order to understand this difference between Figure 10a and the observed data, we note that the solutions represented here span a range of $2.4 < \Delta\Phi_p/\Phi_{p0} < 94$, where $\Delta\Phi_p$ and $\Phi_{p0} = 1.1 \times 10^{21}$ Mx are the total poloidal flux injected and the initial poloidal flux of the flux rope, respectively. In Figure 10b, we have plotted only those speed-height curves corresponding to solutions with $\Delta\Phi_p < 25\ \Phi_{p0} = 2.75 \times 10^{22}$ Mx. There are now only 15 curves. This plot more closely resembles Figure 4 and the results of *MacQueen and Fisher* [1983] and is similar to Figure 10 of *Sheeley* [1999].

[101] We return now to the original matrix of 30 solutions (Figure 10a) and impose an observational constraint. We

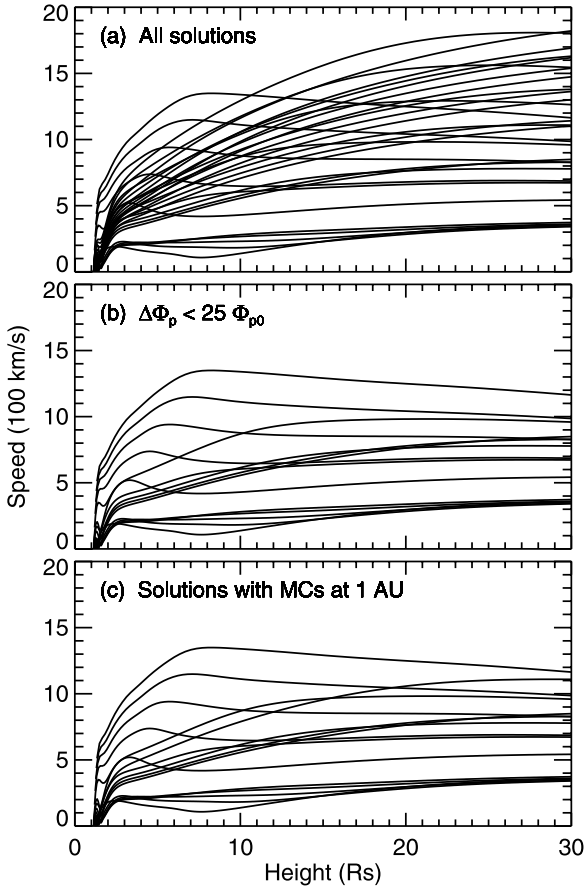

Figure 10. Synthetic speed-height distribution. The input parameters are the poloidal flux injection duration and the total poloidal magnetic energy injected. The ambient coronal field at the initial apex height is B_c = 1 G. The parameters are varied with uniform intervals, with a total of 30 different flux injection profiles. The initial flux rope is identical for all initiation conditions. (a) Includes all solutions. (b) The total injected poloidal flux $\Delta\Phi_p$ is limited to 25 Φ_{p0}. (c) Only those solutions with initial conditions that lead to viable magnetic clouds at 1 AU.

extend each model solution to 1 AU as an initial-value problem and determine the properties of the resulting interplanetary flux rope: the minor radius, speed, magnetic field, density, and temperature. We find that model CMEs with the greatest amounts of injected poloidal flux tend to have stronger magnetic field and are smaller and denser at 1 AU than typical magnetic clouds. We choose only those solutions whose 1 AU properties are consistent with those of observed magnetic clouds. For our discussion, we regard as viable magnetic clouds those model flux ropes at 1 AU with maximum $B < 60$ nT, width $2a > 0.1$ AU, and average proton density $\overline{n} < 35$ cm^{-3}. These values are based on the specific events analyzed by *Burlaga et al.* [1981, 1987, 1998], *Klein and Burlaga* [1982], *Farrugia et al.* [1993], and *Vandas et al.* [1993] and are limited to clouds for which all four quantities (cloud size, peak magnetic field, $\overline{n}$, proton temperature) have been published. A graphical summary of these values is given by *Krall et al.* [2000, Figure 12]. The speed-height curves of these solutions are shown for C2-C3 heights in Figure 10c. We find that the population of flux ropes in Figures 10b and 10c overlap with one exception. This exceptional curve has $\Delta\Phi_p/\Phi_{p0}$ = 27 and lies just outside of the constraint ($\Delta\Phi_p/\Phi_{p0} < 25$) used in Figure 10b.

[102] To consider the possibility that differing types of events in the previous classification of impulsive versus gradual events correspond to differing initial flux rope sizes, we repeated this parameter study with a smaller flux rope, $Z = 5 \times 10^4$ km and $S_f = 1.5 \times 10^5$ km. Here the injected energy ranged from 5×10^{30} to 5.5×10^{31} ergs. While the main acceleration phase occurs on a smaller height scale, the results (not shown) were qualitatively similar to those of Figure 10, yielding a distribution similar to Figures 10b and 10c when the respective flux-limited and magnetic-cloud constraints were imposed. For the sample of smaller flux ropes, the initial flux ($\Phi_0 = 2.6 \times 10^{20}$ Mx) and the resulting flux injection limit ($\Delta\Phi_p < 60\Phi_{p0} = 1.6 \times 10^{22}$ Mx) were both smaller.

[103] We conclude that the main and residual phases are universal and that the previous impulsive-gradual classification scheme is an interpretation of the two types of behavior that we now expect to observe in the residual acceleration phase. That is, events that end the main phase with a velocity significantly higher than that of the ambient SW ($V > V_{sw}$) show constant velocity or deceleration, while those that finish the main phase with $V < V_{sw}$ tend to exhibit gradual acceleration.

[104] It is interesting that the population of erupting flux ropes consistent with magnetic clouds at 1 AU corresponds nearly exactly to the population satisfying $\Delta\Phi_p/\Phi_{p0} < 25$. When either constraint is imposed, the speed-height curves at C2-C3 heights exhibit a distribution consistent with Figure 4 and those shown by *MacQueen and Fisher* [1983] and *Sheeley* [1999]. Contrary to the suggestions of *MacQueen and Fisher* [1983] and *Sheeley* [1999], however, one mechanism is sufficient to produce "two populations" of CMEs. For flux ropes of footpoint separations in the range of $S_f \sim 1/4 - 1/2\ R_\odot$, the flux injection mechanism can consistently explain the observed CME dynamics, the observed speed-height distributions, and magnetic clouds if poloidal energy of the order of $10^{31}-10^{32}$ erg is injected on time scales of several hours with a limit imposed on the total amount of injected poloidal flux.

[105] Another aspect of the data that is recovered in Figure 10 is the bunching up of several of the lowest-velocity curves. In the model, this is a result of the coupling of the erupting flux rope to the background solar wind represented by $F_d \propto (V_{sw} - V)|V_{sw} - V|$.

[106] We have reexamined the model results of *Krall et al.* [2001] and found that distinct main and residual acceleration phases as described above exist for each of the best-fit solutions for the 11 CME events, including those that gradually accelerated through the C2-C3 FOV for as long as 24 hours.

[107] The results shown in Figure 10 suggest that there is a limit to the amount of flux that is injected into any given coronal flux rope. Beyond this limit, the resulting expansion is not consistent with the observed range of CME dynamics.

[108] For the initial flux rope of Figure 10, this limit is $\Delta\Phi_p < 2.8 \times 10^{22}$ Mx, and the highest-speed eruption without unrealistically high acceleration for $Z > 15R_\odot$ has

maximum centroid speed of approximately 1500 km s^{-1}. Thus this synthetic distribution does not include CMEs with $V > 2000$ km s^{-1} that are occasionally observed. Since the highest velocity events tend to be associated with active regions, we have again repeated this parameter study, now with the initial ambient magnetic field increased from 1 to 8 G. These results are shown in Appendix A. We find that the model events include only those that previously might have been described as "impulsive," with centroid speeds at 30 $R_\odot$ ranging from 600 to 1900 km s^{-1}.

[109] Our interpretation is that the energy needed to overcome the initial ambient field is large enough that the resulting flux-rope CME almost always completes the main acceleration phase with a high velocity relative to the ambient solar wind (the injected poloidal energy in this study ranged from 9×10^{32} ergs to 1.9×10^{33} ergs). Imposition of a limit on the injected flux (here, $\Delta\Phi_p < 9\Phi_{p0} = 6.6 \times 10^{22}$ Mx) or on the resulting magnetic cloud at 1 AU allows only the velocity profiles that are consistent with the observations (see Appendix A).

[110] These parameter studies raise an interesting question for future research: what is the physical process that limits the amount of poloidal flux that the Sun injects into a given flux rope? In the three sets of model calculations reported here, this limit is of the order of 10^{22} Mx, despite the large range in flux rope parameters and injected energies considered.

6. Early-Time Acceleration: Signatures of Driving Mechanisms?

[111] In the preceding sections, we have identified the main and residual acceleration phases as characteristic observable features of CME acceleration that should be reproduced by any viable model of CMEs.

[112] The theory of flux rope dynamics shows the existence of a universal scaling law governing the acceleration phases: scaled to $Z_* = S_f/2$, all flux-rope CMEs regardless of the eruption speed have acceleration peaks at $Z \gtrsim Z_*$ (equation (13)). Furthermore, the main acceleration occurs below $Z_m \simeq 1.5\chi Z_*$ where we choose $\chi = 2$ (equation (17b)). This means that acceleration-height curves of CMEs, plotted as functions of Z/Z_*, should show similar envelope functions $\hat{k}_R^2$ even for complex main-acceleration profiles. Conversely, these two heights, Z_* and Z_m, or more directly measurable $\tilde{Z}_*$ and $\tilde{Z}_m$ that include the effects of Φ_p^2 and f_R, can be determined from an observed CME acceleration profile. In principle, they can be used to infer the footpoint separation distance, S_f, and tested against the observed footpoints. Recall that all the heights here refer to the centroid of the flux rope, so that in practice, the width of a CME must also be used to deduce the centroid motion from the leading edge motion.

[113] At present, however, it is not known how unique this inference would be because the corresponding properties of the main acceleration phase in other existing models have not yet been discussed or directly compared with observations. Nevertheless, it is possible to discuss different signatures that may be expected from different scenarios based on their underlying physics. We now contrast these properties of CME acceleration with those that may be expected from a number of competing models.

[114] The above scaling law is characteristic of a 3-D flux rope having fixed footpoints and accelerated by the Lorentz self-force, so long as the flux rope is present as the initial structure or is formed early enough in the eruption process. For example, the MHD simulation models of *Linker and Mikić* [1995], *Antiochos et al.* [1999], *Chen and Shibata* [2000], *Amari et al.* [2000], *Linker et al.* [2001], and *Cheng et al.* [2003] hypothesize a magnetic arcade as the initial structure. This class of models is based on the storage-release paradigm, and the initial arcade is transformed into a flux rope via macroscopic reconnection during the eruption. The models differ in detail in the specific manner in which the photospheric footpoints are driven or in the assumed ambient coronal magnetic field. These simulations encompass scenarios based on slow shearing of footpoints of an arcade [*Linker and Miki*, 1995], slow footpoint motion combined with enhanced resistivity in current sheets [*Cheng et al.*, 2003], cancellation of coronal fields by newly emerging flux [e.g., *Amari et al.*, 2000; *Chen and Shibata*, 2000; *Linker et al.*, 2001] such as may be applicable to the suggestion of *van Ballegooijen and Martens* [1989], and reconnection between the sheared arcade and the coronal fields [*Antiochos et al.*, 1999]. Another class of models depends on "fast reconnection" to produce and add flux to a flux rope in an arcade [e.g., *Vršnak*, 1990b; *Forbes and Priest*, 1995]. In the simulation model of [*Wu et al.*, 1999], an initial flux rope is set into motion by increasing the poloidal field, which is equivalent to poloidal flux injection.

[115] In the storage-release models outlined above, the coronal magnetic field of an arcade is converted to the "private" poloidal flux of the flux rope. This is the flux attributable to the current I_t and excludes contributions from currents outside the flux rope. During this process, the private poloidal flux increases from zero or some initial value, Φ_{p0}, to the final value when the flux rope is fully formed. Thus these models implicitly have quantities that are mathematically equivalent to $\Phi_p(t)$ in our formulation. To the extent that a 3-D flux rope is formed prior to the eruption and its motion is described by MHD, the subsequent flux-rope motion is governed by equation (9). The key difference is that the functional form of $d\Phi_p(t)/dt$ in these models, the amount and duration of equivalent "flux injection," is determined by the required macroscopic 3-D reconnection in the corona, which in turn is governed by nonideal MHD effects and the specified photospheric flows. In terms of the equivalent $d\Phi_p/dt$ profile, the reconnection process determines the time constant (λ_1) and the duration of flux injection (δ). By determining the form of equivalent $d\Phi_p/dt$ for these reconnection scenarios, the results of these models can be directly compared with the acceleration physics of the present model and the observed CME acceleration.

[116] At this time, most simulation models are in 2-D or 2.5-D, except for the 3-D simulations of *Amari et al.* [2000], *Linker et al.* [2001], *Tokman and Bellan* [2002], and *Roussev et al.* [2003]. We note that to date, none of the published 3-D simulation results has been directly compared with CME data. However, *Roussev et al.* [2003] carried out a quantitative 3-D simulation of the expansion of a flux rope with fixed (line-tied) footpoints that can be directly compared with our results. The simulation starts with an initial flux rope with the apex at $Z_0 = 8 \times 10^4$ km and footpoint separation of $S_f = 1.96 \times 10^5$ km. After the

eruption, the apex (*O*-point in their Figure 2) attains maximum acceleration at about $t = 6$ min at height $Z \simeq 1.1 \times 10^5$ km. This is slightly higher than $S_f/2$ and is in excellent agreement with our results (section 3.4). We now examine this apparent agreement.

[117] As a model structure, *Roussev et al.* [2003] invoke the equilibrium model of *Titov and Démoulin* [1999], which consists of an axisymmetric torus that is partially submerged below the photosphere. The flux rope is defined by a toroidal field and an overlying poloidal field externally applied by a subphotospheric line current and a pair of magnetic charges, respectively. There are two significant differences between the Roussev et al.'s simulation and the Titov and Démoulin model. First, the Titov-Démoulin model does not constrain the photospheric footpoints to be stationary. Second, in the simulation, the applied toroidal field is set to zero; otherwise, the flux rope does not erupt. Thus any toroidal field in the simulated flux rope is produced by the poloidal current. In contrast to the Titov-Démoulin model, our model flux rope has stationary footpoints and a toroidal field produced by the poloidal current. Therefore the simulation model of *Roussev et al.* [2003] more closely corresponds to the model construct we have adopted than to that of *Titov and Démoulin* [1999].

[118] There are, however, a number of differences between the *Roussev et al.* [2003] simulation system and our model flux rope. In the former, the overlying poloidal field, in our notation, $B_c(z)$, monotonically decreases with height rapidly enough that the initial flux rope is in an unstable equilibrium. In our system, $B_c(z)$ is chosen such that the initial flux rope is in stable equilibrium. Referring to Figure 8 for illustration, a monotonically decreasing B_c profile would yield a $J \times B_c$ curve (curve 2) with a shallower minimum or no minimum at $Z = \tilde{Z}_*$. This difference only quantitatively affects the B_c term in equation (7b) and does not alter the main acceleration properties determined by $k_R^2 \Phi_p^2 f_R$. Another difference is that in the simulation model, the toroidal current J_t is uniform inside the current channel, which gives $\xi_i = 1/2$, as opposed to $\xi_i = 1.2$ for our model. This difference is small and affects only the ξ_i terms in equations (3b) and (7b). The most significant difference between Roussev et al.'s simulation and our model is that the simulation imposes $d\Phi_p/dt = 0$ except for the amount of poloidal flux that is added to the flux rope via reconnection. The centroid acceleration is still given by $d^2Z/dt^2 \propto k_R^2 \Phi_p^2 f_R$ and peaks at $\tilde{Z}_* > Z_*$. We conclude that the good agreement noted above is genuine and that equation (7) correctly describes the net major radial force in the simulation (also see the discussion at the end of section 3.3). For this agreement, it is essential that the preeruption structure is a flux rope with fixed footpoints. It would be interesting to determine the precise and quantitative form of the equivalent $\Phi_p(t)$ function for the simulation model.

[119] Numerically, the simulation of *Roussev et al.* [2003] is defined in a rectangular grid, and the long-time behavior of the flux rope cannot be determined because of the limited simulation domain. Neither limitation, however, affects the k_R^2 factor in equation (12) and the S_f-scaling law during the main acceleration phase, which occurs while the flux rope is far from the simulation boundaries.

[120] In terms of the forces, *Titov and Démoulin* [1999] also use the integrated MHD approach, and their force equation is essentially identical to equation (7). The key difference between the two models is that the footpoints in the Titov-Démoulin model are not constrained so that their model equations do not have the S_f scaling.

[121] The storage-release paradigm, in its conceptual formulation, specifies the component of magnetic field $B_n(\mathbf{x})$ normal to the solar surface and a flow vector $\mathbf{v}(\mathbf{x}, t)$ lying in this surface. In ideal MHD, this boundary condition is equivalent to specifying an electric field in the photosphere, $\mathbf{E}(\mathbf{x}, t) = -\mathbf{v} \times \mathbf{B}/c$. This formulation was articulated by *Gold and Hoyle* [1960] as a mechanism to explain solar flares and has been extended to the modeling of CME eruptions as discussed above. The magnetic energy powering the eruption is converted from the horizontal photospheric motions and transported to the corona through the quasi-static stressing of the coronal magnetic field. In this concept, the Poynting flux at the surface is quasi-static and predominantly horizontal (parallel to specified $\mathbf{v}$). This is in contrast to the hypothesis underlying the present paper in which the Poynting flux P_n associated with the injected poloidal flux passing through the solar surface provides the driver and the bulk of the energy of eruption [*Chen*, 1989]. In this view, the CME phenomenon is simply an MHD relaxation process in which an existing magnetic structure responds to increased magnetic energy, which occurs at $V < V_M$ everwhere [*Chen*, 2001]. The "fast" motions seen in the corona ($\sim$1000 km s^{-1}) correspond to the characteristic speeds of the corona and are perceived to be "eruptive" merely in comparison with the "slow" characteristic speeds in the dense photosphere ($\sim$1 km s^{-1}). Normalized to the local magnetosonic speed and transit time, the equations of motion do not distinguish between the two disparate regions.

[122] The present paper and the earlier comparisons of theory and data show that the erupting flux rope model is able to explain in a physical as well as quantitative manner the observed dynamics of CMEs in the C1-C2-C3 FOV and the interplanetary magnetic clouds. Nevertheless, the hypothesis that eruptions are caused by poloidal flux injection has been criticized. Perhaps the most specific of these criticisms was given by *Forbes* [2001]. The argument is that if the poloidal energy ($\sim 10^{32}$ erg) is injected in 10^3 sec (<1 hour) and if the poloidal field is coherent over 10^{10} km^2, there should be (1) detectable changes in the magnetic field and (2) large-scale photospheric plasma motion in excess of 10 km s^{-1}. However, Figures 1–3 and the solutions found by *Chen et al.* [1997, 2000], *Wood et al.* [1999], and *Krall et al.* [2001] for specific observed CMEs all show that the poloidal flux injection that is required by the model to match the observed dynamics occurs over at least 1 hour, even for rapidly accelerated CMEs, and sometimes over 5–10 hours. Furthermore, these solutions show that the bulk of the acceleration (i.e., the main phase) occurs and is finished early in the flux injection process, usually before $d\Phi_p/dt$ reaches its maximum, corresponding to a relatively small fraction of the total flux to be injected. This is true for all events that we have previously modeled. The injection time of 10^3 sec assumed by *Forbes* [2001] is not derived from the equations of motion of the model and is indeed inconsistent with the demonstrated results of the model. The correct estimate based on the injection times given by the model would correspond to a speed that is one to two orders of magnitude

smaller than the figure of 10 km s^{-1} given by *Forbes* [2001]. As noted earlier, the plasma motion in response to flux injection occurs at the local magnetosonic speed ($\sim$1 km s^{-1}) associated with the (locally horizontal) poloidal field, as illustrated by the wavy curves in Figure 5.

[123] Concerning the second point of *Forbes* [2001] that large slabs of photospheric plasma must move upward, we note that the injection of poloidal field should instead be associated with nonuniform motion of the high-β ($\beta \gg 1$) photospheric plasma. Magnetized plasma motions in such environments are not likely to have correlation lengths of $\sim 10^5$ km and be coherent. This suggests that turbulent broadening of photospheric lines may be a more likely manifestation of flux injection.

[124] Underlying this criticism is the prevailing notion that the photospheric magnetic field does not change in association with eruptions [e.g., *Gold and Hoyle*, 1960]. This argument is based on observation of the longitudinal component of the photospheric magnetic field, which corresponds to the toroidal (i.e., axial) field of the flux rope. In the model, the toroidal field at the photosphere remains unchanged during the eruption. This is consistent with observations of no unusual changes in the vertical field during flares. Rather, injection of poloidal flux primarily alters the horizontal magnetic field at the solar surface. The magnitude of changes in the photospheric poloidal field has not been calculated because the model does not treat the boundary region between the corona and the photosphere.

[125] Observationally, the poloidal field in the photosphere is considerably weaker than the axial field (vertical at the solar surface) and has been difficult to measure with high sensitivity and time-cadence. Nevertheless, there are recent indications [*Spirock et al.*, 2002; *Wang et al.*, 2002] that the tangential flux after very large (X-class) flares can be considerably greater than that prior to the flares. Relative to any given CME, this is only suggestive, but it is significant that both predicted changes and the apparent magnetic field changes associated with large flares are in the tangential component.

[126] At the base of the corona, it is possible to estimate the changes in the poloidal field at the footpoints of the flux rope. Defining $B_{pf}(t) \equiv B_p(t; r = a_f)$ at the footpoints, B_{pf} of a flux rope has been found to increase in tens of minutes by 0–50%, depending on how much and how fast poloidal flux is injected [*Chen*, 1996; *Krall et al.*, 2001]. In actual observations, any measured tangential component will contain contributions from other sources so that the observed field would not asymptote to zero and the fractional change would be smaller. However, we expect the predicted variation in B_{pf} to exhibit measurable temporal relationship with the main acceleration phase. Figure 11 shows $B_{pf}(t)$ (solid curve) normalized to the the initial value $B_{pf}(t = 0)$ for each of the three specific CMEs discussed in the paper. In each panel, the solid vertical line corresponds to the time when the toroidal current $I_t \propto k_R \Phi_p$ is maximum. In all cases, B_{pf} decreases to half the maximum value approximately where the main acceleration phase ends (Figures 1–3). Based on these and earlier results, we expect the poloidal field at the base of the corona to exhibit variations ($\lesssim$50%) during the main acceleration phase.

[127] The toroidal current in the photosphere, however, is determined by subphotospheric properties, which are not

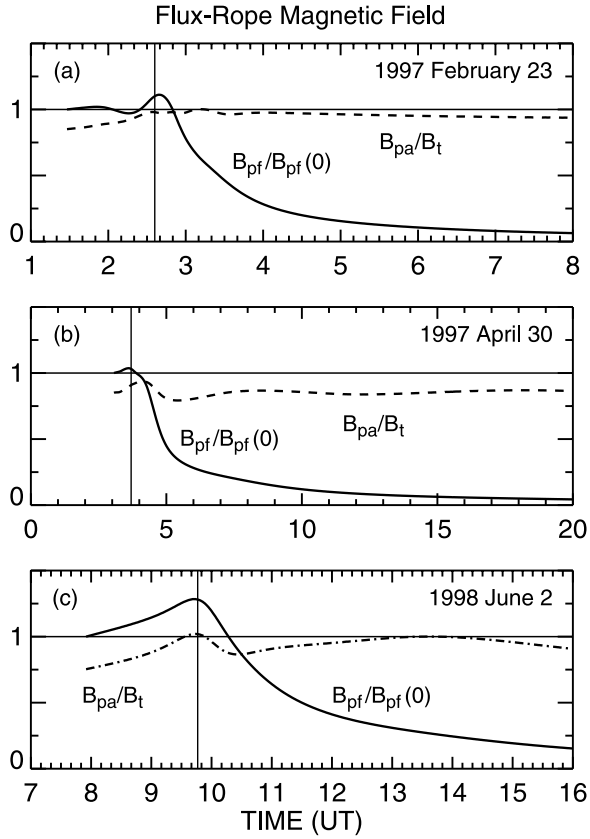

Figure 11. Magnetic field components of the footpoints at the base of the corona. Poloidal $B_{pf} = B_p(t, a_f)$ and toroidal $\overline{B}_{tf}$ components at the footpoints are shown. $B_{pa}/\overline{B}_t$ is the ratio of poloidal and toroidal components at the apex in the corona. $B_{pa}/\overline{B}_t$ is nearly constant in the residual acceleration phase for all three CMEs.

treated in the model. We do expect that in the photosphere, the duration of changes in the poloidal flux should coincide with that of $d\Phi_p/dt$ independently of details. We expect complicated plasma dynamics in the boundary layer between the photosphere (high β) and the base of the corona (low β). As noted above, these processes are beyond the scope of the present model.

[128] Figure 11 also shows the quantity $B_{pa}/\overline{B}_t$ for each of the three CMEs (dashed curves). Because realistic flux ropes do not have uniform magnetic field pitch, we use this quantity as a proxy for the magnetic pitch at the apex. In each event, $B_{pa}/\overline{B}_t$ at the apex is nearly constant except when I_t is maximum. This is because the minor radius expands in near equilibrium [*Chen*, 1989, section III], which gives $\overline{B}_t^2/B_{pa}^2 \simeq 1 - \beta_p \simeq 1$, where β_p is typically negative with $|\beta_p| \sim 0.1$.

[129] Finally, we touch on a point that has received much recent attention in the literature: magnetic helicity. The helicity of a flux rope is $K \propto \Phi_p \Phi_t$ [e.g., *Chen*, 1996, section 5.2], which is a measure of the linked flux. Poloidal flux injection increases Φ_p and therefore K. That is, in our model, the injected helicity is associated with the Poynting flux P_n normal to the surface, which is the dominant contributor to the energy of eruption. This energy is the

external poloidal energy U_{pe} in equation (4a), primarily residing outside the current channel (equation (4b)).

[130] Recently, a number of studies have examined the helicity budget in connection with CMEs [e.g., *Nindos and Zhang*, 2002; *Green et al.*, 2002; *Kusano et al.*, 2002]. In such studies, the line-of-sight magnetograms are used to estimate the horizontal velocity of magnetic footpoints and changes in the magnetic helicity in the corona. It is interesting that these studies conclude that the observed photospheric motions of the magnetic footpoints cannot account for the helicity ejected by the Sun in the form of CMEs, possibly suggesting that photospheric shearing motions are not adequate for building up the stored energy to account for CMEs. *Kusano et al.* [2002] estimate that the Poynting flux and the photospheric shear motion may contribute comparable amounts of magnetic energy to active-region energy budgets. We suggest that the findings of these studies are consistent with the hypothesis that poloidal flux injection is needed to drive CMEs. These issues merit further research.

7. Summary

[131] We have investigated the physics and observable properties of CME acceleration. Where the initial stages of eruption are clearly observed, an acceleration profile exhibits a well-defined period during which the acceleration peaks. This period is referred to as the "main acceleration phase." The main phase is followed by the "residual acceleration phase," exhibiting significantly smaller positive or negative acceleration than that of the main phase. These phases are distinguished by different contributions of forces. A theoretical analysis demonstrates that the main acceleration phase is governed by a universal scaling law determined by the fixed footpoint separation distance, S_f. This scaling law is characteristic of a 3-D flux rope driven by the Lorentz self-force. We have found that the main phase is limited to below $2-3\ R_\odot$ in typical cases, corresponding to $S_f \sim 1/4-1/2\ R_\odot$, but may extend to $3-4\ R_\odot$ if $S_f \sim 1-2\ R_\odot$. This scaling may serve as a diagnostic of the initial magnetic geometry and a discriminator of proposed acceleration mechanisms.

[132] At the beginning of the paper, we posed specific questions raised by observed properties of CME acceleration: (1) what determines the height beyond which a CME exhibits no rapid acceleration, (2) why is the main acceleration of CMEs typically limited to below 2–3 solar radii, and (3) are distinct mechanisms required to explain the apparent bimodal distribution of speed-height profiles. We offer answers based on the physics of toroidal flux ropes as follows:

[133] 1. The acceleration of a flux-rope CME peaks shortly after the centroid of the apex (Z) reaches the critical height $Z_* \equiv S_f/2$, equation (13). Physically, the curvature of the flux rope and therefore the Lorentz self-force are maximum at this height. This is a 3-D geometrical effect of the toroidal forces. Beyond $Z \simeq Z_*$, the centroid acceleration monotically decreases in magnitude with increasing apex height according to $d^2Z/dt^2 \propto k_R^2 \equiv [R\ln(8R/a_f)]^{-2}$ (equation (12)), diminishing by a factor of χ^{-2} at $Z_m \simeq 1.5\chi Z_*$. This is an inductive property of a 3-D flux rope. These heights provide the scaling dependence, and the actual acceleration is governed by the product $k_R^2\Phi_p^2 f_R$ (equation (12c)) yielding $\tilde{Z}_*$ and $\tilde{Z}_m$, which are more directly determinable from height-time data (section 3.4).

[134] We refer to the acceleration for $Z < Z_m$ as the main acceleration. Acceleration for $Z > Z_m$ is the residual acceleration. We choose $\chi = 2$ to determine the value of Z_m. In addition to being small in magnitude, the residual acceleration varies on a slower time scale τ_R, equation (11).

[135] 2. In answer to questions 1 and 2, the height (Z_*) of maximum acceleration and the height (Z_m) beyond which no significant acceleration is observed are both determined by the footpoint separation distance S_f which is typically less than $1\ R_\odot$. Thus the main acceleration is typically localized to centroid height below $Z_m \simeq 1-2\ R_\odot$ from the photosphere.

[136] 3. Synthetic speed-height curves form a distribution closely resembling those that have been previously reported for CMEs if an upper limit is imposed on the amount of poloidal flux injected into the initial flux rope. This upper limit weakly depends on the strength of the ambient coronal field B_c (section 5 and Appendix A) and on the size of the initial flux rope. In answer to question 3, one driving mechanism is sufficient to explain the apparent bimodal distribution. It is significant that this distribution of CMEs is consistent with the observed parameters of magnetic clouds at 1 AU. For active region flux ropes characterized by strong overlying magnetic fields, acceleration profiles tend to show no "gradual" acceleration high in the corona (Appendix A).

[137] Overall, the main acceleration is predominantly determined by the toroidal Lorentz self-force and the interaction with the overlying magnetic field. In the residual acceleration phase ($Z > Z_m$), drag becomes competitive with the Lorentz self-force. The distinction between "impulsive" and "gradual" CMEs is determined entirely by the absence (impulsive) or presence (gradual) of sustained acceleration in the residual acceleration phase.

[138] In terms of comparing model solutions to observed CMEs, it is necessary to include both the main and residual acceleration phases: the greater the range over which the comparison is made, the stronger the constraint is on the model.

Appendix A: Fast CMEs Associated With Active Regions

[139] Since the highest velocity events tend to be associated with active regions, we consider a stronger overlying field B_c and repeat the study of Figure 10 with the ambient field increased from 1 G to 8 G. The initial flux rope has the same geometry as in Figure 10, with $Z_0 = 1 \times 10^5$ km and $S_f = 3 \times 10^5$ km. The initial force balance condition yields greater initial magnetic flux ($B_t \simeq 50$ G on the axis) and poloidal flux $\Phi_{p0} = 7.3 \times 10^{21}$ Mx. With a higher B_c, however, greater amounts of injected energy are needed to overcome the restoring force exerted by B_c given by the B_c/B_{pa} term in equation (7). Accordingly, we increase the amounts of injected poloidal energy to 9, 11, 13, 15, 17, and 19×10^{32} ergs. We use the identical functional form of $d\Phi_p/dt$ and flux-injection time durations as in Figure 10 (1, 3, 5, 7, and 9 hours). For injected energy less than 9×10^{32} ergs, the flux rope failed to overcome B_c and erupt. In

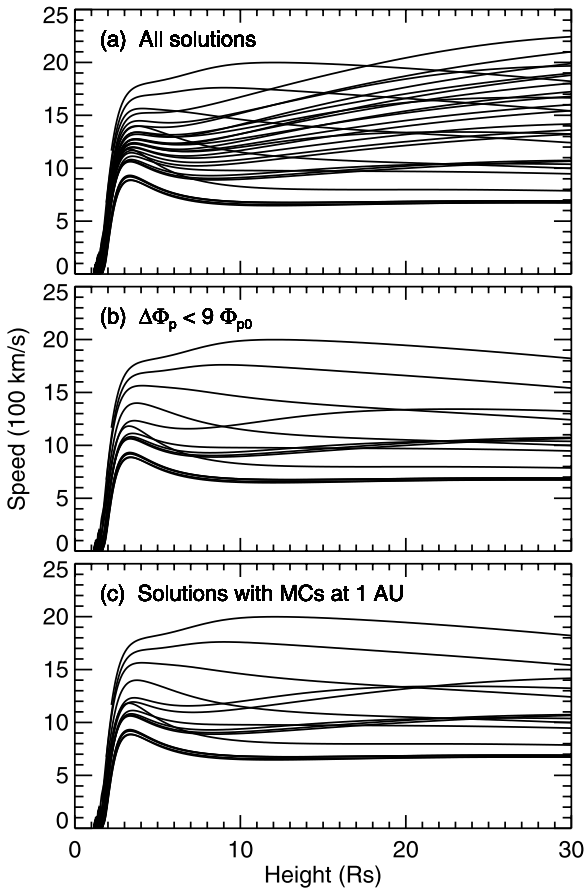

Figure 12. Synthetic speed-height distribution. The initial flux rope is the same as that in Figure 10, but the ambient coronal field is B_c = 8 G at the initial apex height. The parameters are varied with uniform intervals, with a total of 30 different flux injection profiles. (a) Includes all solutions. (b) The total injected poloidal flux $\Delta\Phi_p$ is limited 9 Φ_{p0}. (c) Only those solutions with initiation conditions that lead to viable magnetic clouds at 1 AU.

such cases, the flux rope simply rises and reaches an equilibrium at a greater height. All 30 eruptive solutions are shown in Figure 12a. As in Figure 10a, some solutions show large and sustained acceleration above $Z = 5\ R_\odot$. What is not present in this plot is the family of "gradual" events seen in all panels of Figure 10. The large Lorentz force required to overcome the restraining influence of the ambient field B_c tends to rule out such events except in special cases where the driving force is only slightly greater than the restoring force.

[140] The form of the overlying field profile, $B_c(z)$, also affects the speed profile: the rapid acceleration evident for heights below $\sim$3 $R_\odot$ in Figure 12 occurs at slightly lower heights if $B_c(z)$ is assumed to fall off more rapidly. The model does not include self-consistent interaction between the expanding flux rope and the coronal B_c field. However, the most important aspect of B_c in terms of producing the population of fastest CMEs (Figure 12) versus the slower population (Figure 10) is its influence on the magnetic field of the initial flux rope that can be maintained in equilibrium by B_c. This is an equilibrium property, unaffected by the lack of self-consistent interaction.

[141] If we plot only the solutions in which the amount of flux injected is limited to $\Delta\Phi_p < 9\Phi_{p0} = 6.6 \times 10^{22}$ Mx, we obtain the 15 curves shown in Figure 12b. If we similarly plot only the solutions which produce magnetic-cloud-like flux ropes at 1 AU, we obtain a nearly identical set of 16 curves shown in Figure 12c. Thus together with Figures 10b and 10c, we recover model eruptions that are consistent with the observed distribution of CME speeds, including events consistent with the highest-speed observed events. Since CMEs with centroid velocities greater than 2000 km s^{-1} are rare, the results imply that there is a natural limit to the ambient magnetic field strength or to the poloidal energy that is injected. Based on the observational knowledge of the coronal magnetic environment and the observed CME dynamics, we expect that the set of model eruptions in Figure 12 is already near or at the upper limit of injected magnetic energy for realistic CMEs.

[142] **Acknowledgments.** We acknowledge valuable discussions with I. Roussev of the University of Michigan. We are grateful to the National Solar Observatory at Kitt Peak, Arizona for the use of the magnetogram data (Figure 7c), and to Haimin Wang of New Jersey Institute of Technology for providing the Hα image (Figure 6a) and enhancing the Kitt Peak magnetogram (Figure 7c). This work was supported by the Office of Naval Research (ONR) and the National Aeronautics and Space Administration (NASA). The SOHO LASCO and EIT data used here produced by a consortium of the Naval Research Laboratory (USA), Max-Planck-Institüt für Aeronomie (Germany), Laboratoire d'Astronomie (France), and the University of Birmingham (UK). SOHO is a project of international cooperation between ESA and NASA.

[143] Shadia Rifai Habbal thanks Bojan Vršnak and Pascal Demoulin for their assistance in evaluating this paper.

References

Alexander, D., T. R. Metcalf, and N. V. Nitta, Fast acceleration of a CME-related X-ray structure in the low solar corona, *Geophys. Res. Lett.*, *29*, 41, 2002.

Antiochos, S. K., C. R. DeVore, and J. A. Klimchuk, A model for solar coronal mass ejections, *Astrophys. J.*, *510*, 485, 1999.

Amari, T., J. F. Luciani, Z. Mikić, and J. Linker, A twisted flux rope model for coronal mass ejections and two-ribbon flares, *Astrophys. J.*, *529*, L49, 2000.

Brueckner, G. E., et al., The large angle spectroscopic coronagraph (LASCO), *Sol. Phys.*, *162*, 357, 1995.

Burlaga, L. F., E. Sittler, F. Mariani, and R. Schwenn, Magnetic loop behind an interplanetary shock: Voyager, Helios, and IMP 8 observations, *J. Geophys. Res.*, *86*, 6673, 1981.

Burlaga, L. F., K. W. Behanon, and L. W. Klein, Compound streams, magnetic clouds, and major geomagnetic storms, *J. Geophys. Res.*, *92*, 5725, 1987.

Burlaga, L. F., et al., A magnetic cloud containing material: January 1997, *J. Geophys. Res.*, *103*, 277, 1998.

Cargill, P. J., J. Chen, and D. A. Garren, Oscillations and evolution of curved current-carrying loops in the solar corona, *Astrophys. J.*, *423*, 854, 1994.

Chen, J., Effects of toroidal forces in current loops embedded in a background plasma, *Astrophys. J.*, *338*, 453, 1989.

Chen, J., Theory of prominence eruption and propagation: Interplanetary consequences, *J. Geophys. Res.*, *101*, 27,499, 1996.

Chen, J., Physics of coronal mass ejections: A new paradigm of solar eruptions, *Space Sci. Rev.*, *95*, 165, 2001.

Chen, J., and D. A. Garren, Interplanetary magnetic clouds: Topology and driving mechanism, *Geophys. Res. Lett.*, *20*, 2319, 1993.

Chen, P. F., and K. Shibata, An emerging flux trigger mechanism for coronal mass ejections, *Astrophys. J.*, *545*, 524, 2000.

Chen, J., R. A. Howard, G. E. Brueckner, R. Santoro, J. Krall, S. E. Paswaters, O. C. St. Cyr, R. Schwenn, P. Lamy, and G. M. Simnett, Evidence of an erupting magnetic flux rope: LASCO coronal mass ejection of 1997 April 13, *Astrophys. J.*, *490*, L191, 1997.

Chen, J., R. A. Santoro, J. Krall, R. A. Howard, R. Duffin, J. D. Moses, G. E. Brueckner, J. A. Darnell, and J. T. Burkepile, Magnetic geometry

and dynamics of the fast coronal mass ejection of 1997 September 9, *Astrophys. J.*, *533*, 481, 2000.
Cheng, C. Z., Y. Ren, G. S. Choe, and Y.-J. Moon, Flux rope acceleration and enhanced magnetic reconnection rate, *Astrophys. J.*, *596*, 1341, 2003.
Dere, K. P., et al., EIT and LASCO observations of the initiation of a coronal mass ejections, *Solar Phys.*, *175*, 601, 1997.
Dere, K. P., G. E. Brueckner, R. A. Howard, D. J. Michels, and J. P. Delaboudiniere, LASCO and EIT observations of helical structure in coronal mass ejections, *Astrophys. J.*, *516*, 465, 1999.
Forbes, T. G., The role of the photosphere during solar eruptions (abstract), *Eos Trans. AGU*, *82*(20), Spring Meet. Suppl., SH41C-03, 2001.
Forbes, T. G., and E. R. Priest, Photospheric magnetic field evolution and eruptive flares, *Astrophys. J.*, *446*, 377, 1995.
Farrugia, C. J., L. F. Burlaga, V. A. Osherovich, I. G. Richardson, M. P. Freeman, R. P. Lepping, and A. J. Lazarus, A study of an expanding interplanetary magnetic cloud and its interaction with the Earth's magnetosphere: The interplanetary aspect, *J. Geophys. Res.*, *98*, 7621, 1993.
Gallagher, P. T., G. R. Lawrence, and B. R. Dennis, Rapid acceleration of a coronal mass ejection in the low corona and implications for propagation, *Astrophys. J.*, *588*, L53, 2003.
Garren, D. A., and J. Chen, Lorentz self-forces on curved current loops, *Phys. Plasmas*, *1*, 3425, 1994.
Gold, T., and F. Hoyle, On the origin of solar flares, *Mon. Not. R. Astron. Soc.*, *120*, 89, 1960.
Gopalswamy, N., A. Lara, R. P. Lepping, M. L. Kaiser, D. Berdichevsky, and O. C. St. Cyr, Interplanetary acceleration of coronal mass ejections, *Geophys. Res. Lett.*, *27*, 145, 2000.
Gosling, J. T., E. Hildner, R. M. MacQueen, R. H. Munro, A. I. Poland, and C. L. Ross, The speeds of coronal mass ejection events, *Sol. Phys.*, *48*, 389, 1976.
Green, L. M., M. C. López Fuentes, C. H. Mandrini, P. Dmoulin, L. van Dreil-Gesztelyi, and J. L. Culhane, The magnetic helicity budget of a CME-prolific active region., *Solar Phys.*, *208*, 43, 2002.
Howard, R. A., N. R. Sheeley Jr., M. J. Koomen, and D. J. Michels, Coronal Mass Ejections: 1979–1981, *J. Geophys. Res.*, *90*, 8173, 1985.
Kahler, S. W., R. L. Moore, S. R. Kane, and H. Zirin, Filament eruptions and the impulsive phase of solar flares, *Astrophys. J.*, *328*, 824, 1988.
Klein, L. W., and L. F. Burlaga, Interplanetary magnetic clouds at 1 AU, *J. Geophys. Res.*, *87*, 613, 1982.
Krall, J., J. Chen, and R. Santoro, Drive mechanisms of erupting solar magnetic flux ropes, *Astrophys. J.*, *539*, 964, 2000.
Krall, J., J. Chen, R. T. Duffin, R. A. Howard, and B. J. Thompson, Erupting solar magnetic flux ropes: Theory and observation, *Astrophys. J.*, *562*, 1045, 2001.
Kusano, K., T. Maeshiro, T. Yokoyama, and T. Sakurai, Measurement of magnetic helicity injection and free energy loading into the solar corona, *Astrophys. J.*, *577*, 501, 2002.
Landau, L. D., E. M. Lifshitz, and L. P. Pitaevskii, *Electrodynamics of Continuous Media*, Pergamon, New York, 1984.
Lin, J., T. G. Forbes, P. A. Isenberg, and P. Démoulin, The effect of curvature on flux-rope models of coronal mass ejections, *Astrophys. J.*, *504*, 1006, 1998.
Linker, J. A., and Z. Mikić, Disruption of a helmet streamer by photospheric shear, *Astrophys. J.*, *438*, L45, 1995.
Linker, J. A., R. Lionello, Z. Mikić, and T. Amari, Magnetohydrodynamic modeling of prominence formation within a helmet streamer, *J. Geophys. Res.*, *106*, 25,165, 2001.
Low, B. C., and J. R. Hundhausen, Magnetostatic structures of the solar corona, II, The magnetic topology of quiescent prominence, *Astrophys. J.*, *443*, 818, 1995.
MacQueen, R. M., and R. R. Fisher, The kinematics of solar inner coronal transients, *Solar Phys.*, *89*, 89, 1983.
Moon, Y.-J., G. S. Choe, H. Wang, Y. D. Park, N. Gopalswamy, G. Yang, and S. Yashiro, A statistical study of two classes of coronal mass ejections, *Astrophys. J.*, *581*, 694, 2002.
Nindos, A., and H. Zhang, Photospheric motions and coronal election productivity, *Astrophys. J.*, *573*, L133, 2002.
Plunkett, S. P., A. Vourlidas, S. Simberova, J. Karlicky, P. Kotrc, P. Heinzel, Y. A. Kupryakov, W. P. Guo, and S. T. Wu, Simultaneous SOHO and ground-based observations of a large eruptive prominence and coronal mass ejection, *Solar Phys.*, *194*, 371, 2000.
Roussev, I. I., T. G. Forbes, T. I. Gombosi, I. V. Sokolov, D. L. DeZeeuw, and J. Birn, A three-dimensional flux rope model for coronal mass ejections based on a loss of equilibrium, *Astrophys. J.*, *588*, L45, 2003.
Shafranov, V. D., Plasma equilibrium in a magnetic field, in *Reviews of Plasma Physics*, vol. 2, edited by M. A. Leontovich, p. 103, Consult. Bur., New York, 1966.
Shanmugaraju, A., Y.-J. Moon, M. Dryer, and S. Umapathy, On the kinematic evolution of flare-associated CMEs, *Solar Phys.*, *215*, 185, 2003.
Sheeley, N. R., Jr., Using LASCO observations to infer solar wind speed near the Sun, in *Solar Wind Nine*, edited by S. R. Habbal et al., *AIP Conf. Proc., 471*, 41, 1999.
Sheeley, N. R., Jr., J. H. Walters, Y.-M. Wang, and R. A. Howard, Continuous tracking of coronal outflows: Two kinds of coronal mass ejections, *J. Geophys. Res.*, *104*, 24,739, 1999.
Spirock, T. J., V. B. Yurchyshyn, and H. Wang, Rapid changes in the longitudinal magnetic field related to the 2001 April 2 X20 flare, *Astrophys. J.*, *572*, 1072, 2002.
Srivastava, N., R. Schwenn, B. Inhester, S. F. Martin, and Y. Hanaoka, Factors related to the origin of a gradual coronal mass ejection associated with an eruptive prominence on 1998 June 21–22, *Astrophys. J.*, *534*, 468, 2000.
St. Cyr, O. C., J. T. Burkepile, A. J. Hundhausen, and A. R. Lecinski, A comparison of ground-based and spacecraft observations of coronal mass ejections from 1980–1989, *J. Geophys. Res.*, *104*, 12,493, 1999.
Titov, S. V., and P. Démoulin, Basic topology of twistedmagnetic configurations in solar flares, *Astron. Astrophys.*, *351*, 707, 1999.
Tokman, M., and P. M. Bellan, Three-dimensional model of the structure and evolution of coronal mass ejections, *Astrophys. J.*, *567*, 1202, 2002.
van Ballegooijen, A. A., and P. C. H. Martens, Formation and eruption of solar prominences, *Astrophys. J.*, *343*, 971, 1989.
Vandas, M., S. Fischer, P. Pelant, and A. Geranios, Spheroidal models of magnetic clouds and their comparison with spacecraft measurements, *J. Geophys. Res.*, *98*, 11,467, 1993.
Vršnak, B., Dynamics and internal structure of an eruptive prominence, *Solar Phys.*, *127*, 129, 1990a.
Vršnak, B., Eruptive instability of cylindrical prominences, *Solar Phys.*, *129*, 295, 1990b.
Vršnak, B., Dynamics of solar coronal eruptions, *J. Geophys. Res.*, *106*, 25,249, 2001.
Vršnak, B., V. Ruždjak, B. Rompolt, D. Roša, and P. Zlobec, Kinematics and evolution of twist in the eruptive prominence of 18 August 1980, *Solar Phys.*, *146*, 147, 1993.
Wang, H., T. J. Spirock, J. Qiu, H. Ji, V. Yurchyshyn, Y.-J. Moon, C. Denker, and P. R. Goode, Rapid changes of magnetic field associated with six X-class flares, *Astrophys. J.*, *576*, 497, 2002.
Wolfson, R., and S. Saran, Energetics of coronal mass ejections: Role of the streamer cavity, *Astrophys. J.*, *499*, 496, 1998.
Wood, B. E., M. Karovska, J. Chen, G. E. Brueckner, J. W. Cook, and R. A. Howard, Comparison of two coronal mass ejections observed by EIT and LASCO with a model of an erupting magnetic flux rope, *Astrophys. J.*, *512*, 484, 1999.
Wu, S. T., W. P. Guo, D. J. Michels, and L. F. Burlaga, MHD description of the dynamical relationship between a flux rope, streamer, coronal mass ejection, and magnetic cloud: An analysis of the January 1997 Sun-Earth connection event, *J. Geophys. Res.*, *104*, 14,789, 1999.
Zhang, J., K. P. Dere, R. A. Howard, M. R. Kundu, and S. M. White, On the temporal relationship between coronal mass ejections and flares, *Astrophys. J.*, *559*, 452, 2001.

J. Chen and J. Krall, Plasma Physics Division, Naval Research Laboratory, Code 6790, Washington, DC 20375, USA (chen@ppd.nrl.navy.mil; krall@ppdmail.nrl.navy.mil)